Tumor edge architecture in glioblastoma is constructed by inter-cellular signals from vascular endothelial cells

Authors:

Soniya Bastola[1, 5]†, Marat S. Pavlyukov[2]†, Yasmin Ghochani[3], Sree Deepthi Muthukrishnan[3], Hee Jin Cho[4], Yeri Lee[4], Alireza Sohrabi[5], Stephanie K. Seidlits[5, 6], Daisuke Yamashita[7], Min Soo Kim[1, 3], Ksenia S. Anufrieva[8], Riki Kawaguchi[9], Yue Qin[9], Alma L Burlingame[10], Juan A. Oses-Prieto[10], Steven A. Goldman[11], Anita B. Hjelmeland[12], Do-Hyun Nam[13], Harley I. Kornblum[1, 15]*, and Ichiro Nakano[5, 14, 15]*

Affiliations:

[1]Graduate Biomedical Sciences, University of Alabama at Birmingham, AL 35294, USA

[2]Shemyakin-Ovchinnikov Institute of Bioorganic Chemistry, Moscow 117997, Russia

[3]The Intellectual and Developmental Disabilities Research Center, The Semel Institute for Neuroscience and Human Behavior, and The Broad Stem Cell Research Center, The Jonsson Comprehensive Cancer Center, David Geffen School of Medicine at UCLA, Los Angeles, CA 90095, USA

[4]Research Institute for Future Medicine, Samsung Medical Center, Seoul 06351, Korea

[5]Department of Bioengineering, University of California, Los Angeles, Los Angeles, CA 90095, USA

[6]Jonsson Comprehensive Cancer Center, Broad Stem Cell Research Center, Brain Research Institute, University of California, Los Angeles, Los Angeles, CA 90095, USA

[7]Department of Neurosurgery, Ehime University, Japan

[8]Center for Precision Genome Editing and Genetic Technologies for Biomedicine, Federal Research and Clinical Center of Physical-Chemical Medicine of Federal Medical Biological Agency, Moscow, Russia

[9]Semel Institute for Neuroscience and Human Behavior, Departments of Psychiatry and Neurology, David Geffen School of Medicine, University of California, Los Angeles, CA, 90095, USA

[10]Department of Pharmaceutical Chemistry, University of California, San Francisco, San Francisco CA 94158, USA

[11]Center for Translational Neuromedicine, University of Rochester Medical Center, Rochester, NY, 14642, USA; and Faculty of Health and Medical Sciences, University of Copenhagen, Copenhagen 2200, Denmark
[12]Department of Cell, Developmental and Integrative Biology, University of Alabama at Birmingham, Birmingham, AL 35294 USA
[13]Department of Neurosurgery, Samsung Medical Center, Sungkyunkwan University School of Medicine, Seoul, Korea; Department of Health Science & Technology, Samsung Advanced Institute for Health Science & Technology, Sungkyunkwan University, Seoul, Korea.
[14]Research and Development Center for Precision Medicine, Tsukuba University 305-8550 Japan
[15*] Lead Contact
†These authors contributed equally to this work

***Correspondence:**

Ichiro Nakano, MD, PhD

Research and Development Center for Precision Medicine, Tsukuba University

1-2 Kasuga Tsukuba Ibaragi 305-8550

E-mail: nakano.ichiro.fw@u.tsukuba.ac.jp

Harley Kornblum, MD, PhD

Departments of Psychiatry, Pharmacology, and Pediatrics, David Geffen School of Medicine at UCLA, Los Angeles, CA 90095, USA

E-mail: hkornblum@mednet.ucla.edu

Key words: glioblastoma, vascular endothelial cells, endocan, ESM1, tumor heterogeneity

Running Title:

Vascular endothelial cell-controlled spatial identity for glioblastoma edge region

Abstract

Glioblastoma is a lethal brain cancer with active infiltration of tumor cells at the periphery where the vascular supply is enriched to create its own niche. Given that tumor recurrence is predominantly local, most of the seeds for lethal recurrence are hidden at the tumor edge and are surgically inaccessible. Here, we found that the spatial identity of the edge-located glioblastoma cells is, in the tested models, constructed by inter-cellular signals derived from the soluble factor endocan (protein product of *Esm1*) that is secreted by tumor-associated vascular endothelial (VE) cells. Injection of two distinct mouse glioblastoma models into *Esm1* knockout (KO) mice resulted in tumors that failed to form typical edge lesions, resulting in the formation of compact core-only lesions. In sharp contrast, tumors derived in WT (*Esm1*-intact) mice harbored both tumor core and edge structures. Despite these obvious phenotypic differences, the aggressiveness of these two tumor types was indistinguishable *in vivo.* Surprisingly, regardless of the host system, co-injection of mixture of these two tumor subpopulations gave rise tumors with much worse survival, indicating that the accumulating tumor cell heterogeneity contributes to elevate malignancy. Mechanistically, endocan competes with PDGF to bind and activate PDGFRα in human glioblastoma cells, accompanied with the upregulation of the *Myc* transcriptional activity *via* alterations in its promoter chromatin structure. One of the mainstays of glioblastoma treatment, radiation, induces endocan secretion from VE cells, which promotes the radioresistance of the edge-located glioblastoma cells, allowing for the persistence of the edge structure. Collectively, these data suggest that intra-tumoral spatial heterogeneity is initiated by the VE cell-derived endocan signals through PDGFRα to construct tumor edge-to-core (E-to-C) architecture to cause lethal tumor recurrence.

88 **Introduction**

89 Glioblastoma is a devastating intraparenchymal brain cancer with the hallmarks of peripheral
90 hypervascularity and a high degree of intra-tumoral cellular and molecular heterogeneity.
91 Surgical resection is limited in its curative potential due to the inability to completely eradicate
92 tumor cells from the brain [1-3]. These post-surgical residual tumor cells are primarily located at
93 the tumor edge (defined by the non-enhancing T2-FLAIR positive area on MRI, see **Figures 1A,**
94 **S1A and B** for the definition of tumor edge). The unique ecosystem at the tumor edge is
95 composed predominantly of functioning brain parenchymal cells with scattered tumor cells
96 harboring rich vasculature. Thus, even with the ongoing attempt towards supra-total resection of
97 glioblastomas designed to remove edge lesions in non-eloquent areas of the brain beyond the
98 current standard core resection, the complete removal of tumor cells from the brain may not be
99 a practically attainable goal. Subsequently, a majority of patients inevitably suffer from post-
100 surgical lethal tumor recurrence with reconstruction of the tumor architecture with the core
101 lesions [4-6]. Some of the residual edge-located tumor cells initiate this process, indicating that
102 there is an edge-to-core (E-to-C) progression. In patient-derived pre-clinical glioblastoma
103 models, this E-to-C phenotypic shift was observed particularly in tumor-initiating cells (TICs),
104 and the E-to-C molecular signature was tightly associated with poorer prognosis of glioblastoma
105 patients [4, 7]. We theorize that this E-to-C shift in post-surgical brains is a key determinant of
106 tumor lethality.

107 Because of its accessibility, tumor core tissues (defined by the entire area within the
108 Gadolinium-enhancing lesion on MRI; **Figures 1A, S1A and B**) likely represent the dominant
109 source of the current molecular profiling studies (e.g. The Cancer Genome Atlas (TCGA) and
110 Rembrandt). In recent years, however, several studies have started to gain molecular
111 information about tumor cells at the edge located outside the area of contrast enhancement [8-
112 10]. Likewise, through the collection of subcortical edge tissues from the non-eloquent deep

113 white matter during supra-total resection during awake procedures, we have molecularly
114 characterized the edge- and core-located glioblastoma cells. Evaluation of their transcriptome,
115 metabolome and kinome has revealed their distinctly-activated key molecules (e.g. Bruton's
116 tyrosine kinase, Nitrogen metabolism) [5, 11, 12]. More importantly, their phenotypic differences
117 have been revealed with the established tumor edge and core models derived from patient
118 tumors, suggesting the presence of cell-intrinsic mechanisms for the spatial identities of
119 individual tumor cells.

120 The tumor ecosystem is defined by cooperation and competition among different cell
121 types within the tumor microenvironment. Recently, we identified two sets of intercellular signals
122 associated with the spatially-distinct glioblastoma ecosystem: one derived from dying tumor
123 cells providing growth-promoting and therapy-refractory signals to the near-by surviving tumors
124 cells (most actively in the tumor core) [13] and the other from tumor core cells promoting
125 radioresistance of their edge counterparts [5]. At the tumor edge, perivascular niches are a
126 fertile environment for glioblastoma cells, including TICs, owing in part to the support of vascular
127 endothelial (VE) cells [14, 15]. Various paracrine factors are provided by VE cells to maintain
128 tumor-initiating properties and enhance therapy resistance of glioblastoma cells [14, 16-20].
129 Given that the tumor vasculature is predominantly enriched at tumor edge, we hypothesized that
130 VE cell-driven signals contribute to create “edge-ness” and sought to determine factors
131 elaborated by VE cells that could instruct tumor cells in their intra-tumoral spatial positioning.
132 One of the factors that we identified in this study is endocan, a 20 kDa dermatan sulfate
133 proteoglycan protein encoded by the *Esm1* gene [21]. Prior studies demonstrate that endocan is
134 regulated by hypoxia/VEGF pathway and is a marker of endothelial cell activation, endothelial
135 dysfunction during angiogenesis, and has been shown to be linked to tumor progression [22,
136 23]. The expression of endocan has been correlated with higher grade and shorter survival in
137 glioma, and it has been notably detected in tumor margin [24]. However, the functional role of

138 endocan in glioblastoma remains unknown and therefore endocan has not been evaluated as a
139 therapeutic target even in experimental settings [24, 25].
140 In this study, we sought to uncover whether soluble factors including endocan from VE
141 cells have an instructive role in establishing the structural tumor heterogeneity, possibly
142 originating in the surgically-unresectable tumor edge, to then create the lethal tumor core
143 lesions in glioblastoma.
144
145
146 **Results**
147 **Tumor-associated VE cells promote glioblastoma aggressiveness in vivo, accompanied**
148 **by their secretion of endocan**
149 We first tested whether VE cells promote aggressiveness of glioblastomas in mouse brains by
150 using two VE cell models; one was a short-term primary culture with glioblastoma patient-
151 derived VE cells (TEC15) and the other was an immortalized brain VE cell line (HBEC-5i)
152 (**Figure S2B**). When these VE cells were co-injected with the patient-derived glioma sphere line
153 g1051x –a line that creates tumors in mouse brains harboring both core and edge phenotypes
154 [5] - at a 1:10 ratio into SCID mice, the survival of these mice was significantly shorter than the
155 control group in which g1051x was injected alone (**Figures 1B and S2C**).
156 Immunohistochemistry (IHC) of the co-injection group showed elevated expression of both
157 human and mouse CD31, indicating their possible conjoined role in promoting tumorigenesis in
158 these models (**Figure S2D**).
159 To identify potential trophic factors that could be elaborated by tumor-associated VE
160 cells, we isolated $CD31^+$ tumor-associated VE cells from 8 glioblastoma cases along with non-
161 cancerous $CD31^+$ cells from 5 craniotomies for epilepsy as controls. RNA-sequencing (RNA-
162 seq) analysis revealed *ESM1* (gene encoding the endocan protein) as the second most

163 significantly upregulated gene (FC=9.76, FDR-corrected *p*-value=0.0031) in tumor-derived
164 CD31$^+$ cells compared to the non-neoplastic counterparts (**Figures 1C and 1D)**. In both TCGA
165 and the Samsung Medical Center (SMC) brain tumor databases, *ESM1* expression was found
166 to directly correlate with higher glioma grade, with significant elevation noted in Grade IV
167 glioblastomas (**Figures 1E and 1F**). Survival analysis of glioma patients demonstrated that
168 patients with high level of endocan protein had significantly shorter survival (**Figure 1G**). Given
169 these clinical data, we then investigated whether endocan is secreted from VE cells. ELISA with
170 CM from HBEC-5i cells, normal human astrocytes (NHA), and three glioma sphere lines (g157,
171 g711, and g1051) exhibited significantly higher concentrations (>100pg/ml) of endocan
172 exclusively secreted from HBEC-5i VE cell (**Figure 1H**). We further confirmed that tumor
173 associated CD31$^+$ VE cells express endocan in the perivascular areas of our glioblastoma
174 clinical samples detected by immunofluorescence (**Figure 1I**).
175

176 **Endocan is required for establishing the hypervascular tumor edge structure in murine**
177 **glioblastoma**

178 We next investigated whether endocan plays a role in the establishment of the hypervascular
179 tumor edge and/or core lesions. We utilized wild-type (WT) and *Esm1* knockout (*Esm1* KO)
180 mice [26] as host systems for a tumor challenge. Of note, untreated *Esm1* KO mice did not have
181 any apparent phenotype and the brain vasculature appeared to be normal (**Figure S3A**). We
182 first used freshly-resected murine glioblastoma-like tumor cells isolated from tumors induced by
183 RCAS-PDGAB injection into Nestin-Tva/Cdkn2a-/- mice [27]. Following dissociation into single
184 cells, these murine tumors were then directly injected into the brains of WT and *Esm1* KO mice.
185 The resultant tumors in WT mice (termed WTD tumors) exhibited numerous intra-tumoral
186 hemorrhages in sharp contrast to grayish necrotic tumors in *Esm1* KO mice (*Esm1* KOD
187 tumors) (**Figure 2A**). This difference was reflected by overtly fewer CD31$^+$ VE cells in *Esm1*

188 KOD tumors as compared to WTD tumors (**Figure 2B**). We then utilized another mouse
189 glioblastoma model derived from mice harboring mutations in *p53*, *PTEN*, and *NF1*, termed as
190 mg7080 [28]. *In vitro* glioma sphere cultures enriching for their TIC subpopulation [29] were
191 established from these tumors (**Figure 2C**) and injected into WT and *Esm1* KO mice. IHC for
192 CD31 also displayed a similar difference in vascularity, exhibiting hyper-vascular tumors in the
193 WT animals and hypo-vascular tumors in the *Esm1* KO ones (**Figure 2D**)**.** At the ultrastructural
194 level evaluated by electron microscopy, mg7080-derived WTD blood vessels exhibited an
195 irregular basement membrane, typical of human glioblastoma, while the few blood vessels
196 detected KOD tumors showed a more regular basement membrane (**Figure 2E**). Collectively,
197 these data indicate that endocan secreted by VE cells instructs intratumoral vascular
198 heterogeneity by creating vascular-rich tumor edge lesions.
199
200 **Endocan-driven edge+core and endocan-depleted core lesions cooperatively increase**
201 **intratumoral heterogeneity, elevating the malignancy of murine glioblastoma**
202 Given the remarkable phenotypic difference in tumors with or without endocan in the host brain,
203 we tested whether *Esm1* WTD and KOD cells maintain their phenotypes in the same brain
204 microenvironment. Short-term mg7080 TIC-enriched sphere cultures from WT and KO mice
205 were labeled with GFP- and mCherry-carrying lentivirus, respectively (**Figure 3A**). First, these
206 tumor cells were intracranially co-injected into brains of WT BL/6 mice. IHC with anti-GFP and
207 anti-mCherry antibodies demonstrated that the majority of mCherry-labeled KOD cells remained
208 at the injection site, expanding to create characteristic tumor core lesions. In contrast, GFP-
209 labeled WTD cells were widely distributed within the brain including the injection site (core
210 lesion), as well as distant areas particularly in the corpus callosum and adjacent to the lateral
211 ventricles, resembling the subcortical infiltrating pattern frequently seen in patients'
212 glioblastomas (**Figure 3B, right panel**). This difference was unlikely due to differences in their

213 migration potential since the *in vitro* migration assay using patient derived GBM spheres with
214 and without endocan showed no noticeable difference by adding endocan into the culture
215 (**Figure S3B**). As expected, CD31 staining indicated that the core lesion predominantly formed
216 by KOD cells were hypovascular, while the edge lesion created mainly by WTD cells were
217 hypervascular (**Figures 3C and 3D**). These data suggest that KOD cells have lost their capacity
218 to develop the typical tumor edge structure even in the presence of endocan in the brain,
219 possibly due to lack of some receptor allowing for processing the response to endocan-driven
220 signals. In turn, when this co-injection was performed in *Esm1* KO mice, both GFP^+ WTD and
221 $mCherry^+$ KOD cells remained at or near the injection site, resulting in a compact tumor core
222 lesion without a typical infiltrative hypervascular edge, suggesting that even WTD cells can only
223 create the core lesion with a loss of the capacity to develop edge lesions – similar to the
224 phenotype of KOD tumor (**Figure 3E**). Surprisingly, the survival outcomes of these models
225 showed striking differences: despite the substantial difference in tumor vascularity and
226 localization, the survival of *Esm1* WTD and KOD single injection groups did not show any
227 noticeable difference irrespective of the host system (either WT or *Esm1* KO mice). In contrast,
228 the co-injection group exhibited significantly shorter survival when injected into both WT and
229 *Esm1* KO mice, despite their striking phenotypic differences in these genetically-distinct mouse
230 hosts (**Figures 3F and 3G**). Collectively, these data suggest that, as the ancestor-like tumor
231 subpopulation, endocan-dependent tumor cells harbor the capacity of forming tumor edge and
232 core lesions, giving rise to endocan-depleted tumor cells as their daughter-like progeny
233 population that have lost the capacity to establish edge lesions. However, regardless of the
234 endocan status in the host, these two tumor subpopulations evolve to establish more
235 aggressive, heterogeneous tumors.
236
237 **Endocan binds to and phosphorylates PDGFRα in human glioblastoma cells**

238 Next, we sought to identify the receptor for endocan in glioblastoma cells. We first purified
239 proteins from the plasma membrane of the well-characterized human glioma sphere line g157
240 [30] and incubated these proteins with immobilized endocan. Subsequent elution of bound
241 proteins followed by mass spectrometry unexpectedly identified PDGFRα as a potential
242 endocan-interacting protein (**Figure 4A**). To confirm these data in a cell-free system, we tested
243 the interaction of the corresponding recombinant proteins. Immunoprecipitation experiments
244 demonstrated physical interaction between F_c-tagged PDGFRα and His-tagged endocan
245 (**Figure 4B)**. As another validation, we used the proximal ligation assay, which showed that
246 rhEndocan induces the dimerization of PDGFRα, indicating that endocan is capable of inducing
247 the initial step in PDGFRα activation [31-33] (**Figure S4A**). To further examine the specificity
248 and binding affinity of endocan's interaction with PDGFRα, we performed a binding competition
249 assay between endocan and PDGFBB, a known major ligand for PDGFRα, labeled with
250 Alexa488 and Alexa647 fluorescent dyes, respectively. rhPDGFBB diminished rhEndocan
251 binding to glioblastoma cells in a concentration-dependent manner; similar data were obtained
252 in the opposite experiment where rhEndocan decreased rhPDGFBB binding. Importantly, we
253 observed that rhEndocan at a 10ug/ml concentration was able to completely displace
254 rhPDGFBB from glioblastoma cells, while rhPDGFBB at the corresponding concentration was
255 able to displace only half of the rhEndocan molecules present (**Figures 4C, and S4B**).
256 Consistent with these data, gene set enrichment analysis (GSEA) of the RNA-seq data with
257 mg7080-derived tumors demonstrated that *Esm1* KOD tumors exhibited downregulation of
258 PDGF-mediated signaling pathway and diminished PI3K/AKT signaling network compared to
259 WTD tumors, suggesting the possibility of cell survival conferred by endocan through PDGF-
260 driven pathways (**Figures S4C and Table S1**). As expected, various vasculature-associated
261 genes (e.g. *PODXL* (podocalyxin), *PECAM1* (Platelet Endothelial Cell Adhesion Molecule),
262 *ACTA2* (Smooth Muscle Actin), *VWF* (Von Willebrand Factor), CLDN*5* (claudin 5)) were also

263 significantly reduced in KOD tumors as compared to WTD ones (**Figure S4D**). Consistent with
264 these experimental data, IHC of patient glioblastomas displayed the presence of endocan^{+} cells
265 within perivascular areas of tumors that are adjacent to PDGFRα^{+} cells (**Figure 4D**).
266 Given that downstream activation through PDGFRα requires receptor
267 autophosphorylation, we further investigated whether the addition of recombinant endocan
268 alters the phosphorylation levels of PDGFRα in glioma spheres *in vitro*; PDGFBB was used as a
269 positive control [34]. In this experiment, g1079 cells were treated with rhEndocan or rhPDGFBB,
270 and phosphorylation of PDGFRα at Y720 was measured by western blotting at different time
271 points. rhEndocan (10 ng/ml) induced appreciable phosphorylation of PDGFRα as early as 15
272 minutes after addition and displayed similar temporal kinetics to that of PDGFBB (**Figure 4E**).
273 rhEndocan treatment also resulted in the phosphorylation of the PDGFRα downstream targets
274 p85α, PI3K, and GSK-3β, further confirming activation of this signaling interaction, along with
275 phosphorylation activities of p-GSK3β and p44/42 MAPK (**Figure 4F**).
276 Given that PDGFRα is a key regulator of glioblastoma aggressiveness and that endocan
277 may function as a gatekeeper to turn on this signaling [35-37], we next investigated whether the
278 elimination of PDGFRα activation produces distinct effects in *Esm1* WT and KO background.
279 We hypothesized that blockade of PDGFRα signaling in the *Esm1* WT background would
280 prevent the formation of endocan-induced tumor edge lesions. To this end, we treated *Esm1*
281 WT and KO mice bearing mg7080−derived tumors with Ponatinib, a kinase inhibitor with
282 relatively high selectivity toward PDGFRα [38]. Ponatinib enhanced the survival only of the
283 tumor-bearing WT, but not *Esm1* KO mice (**Figure 4G**). As indicated by immunostaining with
284 WTD tumors, the treatment resulted in a loss of Myc and Olig2 (both markers associated with
285 tumor edge cells) **(Figure 4H)**. On the other hand, we observed increased expression of p65-
286 NFkB (a marker associated with tumor core cells)（**Figure 4H)**. These results suggest that, in

287 this particular tumor model, the PDGFRα-driven glioblastoma growth *in vivo* is mediated by
288 endocan.
289
290 **Endocan-mediated signaling alters chromatin accessibility in glioblastoma cells,**
291 **including the promoter region of the Myc gene**
292 Given the persistence of edge- and core-related phenotypes even following removal from the
293 brain, we hypothesized that the endocan-PDGFRα signaling could modify some chromatin
294 structure to retain long-term intratumoral spatial identity. To test this possibility, we performed
295 ATAC-seq (Assay for Transposase-Accessible Chromatin sequencing) with *Esm1* WTD and
296 KOD to assess whether and how endocan affects chromatin accessibility [39]. In fact,
297 alterations in chromatin structure were noticeably very focused with only 10 genes identified
298 with significantly different chromatin accessibility in their promoter regions among these tumors
299 (**Figures 5A and Table S2**). To explore the relationship between open chromatin and gene
300 expression levels, we next performed RNA-seq analysis on the same samples and compared
301 the gene expression levels by RNA-seq with the promoter accessibility data by ATAC-seq
302 (**Figures 5B and 5C and Table S3**). Our results highlighted that the *Myc* gene - a downstream
303 target of PDGFRα pathway [40]- was among the few genes with both increased promoter
304 accessibility (open chromatin) and upregulated expression in WTD tumors compared to KOD
305 tumors. In addition, IHC of mg7080 tumors showed higher expression of cMyc in WTD tumors
306 as compared to *Esm1* KOD ones (**Figure 5D**). Taken together, these data suggest that, similar
307 to PDGFRα, endocan regulates the open state of the chromatin structure for the *Myc* promoter
308 region, thereby activating its transcription (**Schema in Figure 5E**).
309
310 **Endocan protects edge-located glioblastoma cells from radiotherapy-induced cell death**
311 ***in vivo***

312 We next sought to determine whether standard glioblastoma treatments of radiation and
313 temozolomide (TMZ) influences endocan production or effects. While both radiation and TMZ
314 induced an elevation of *ESM1* mRNA *in vitro* as measured by qRT-PCR (**Figure S5A and S5B**),
315 a more pronounced elevation of endocan protein was observed in radiated HBEC-5i cells as
316 determined by ELISA (**Figure 6A**). Given these findings, we then investigated whether endocan
317 secreted by VE cells plays a role in radioprotection in glioblastoma cells. We pretreated four
318 patient-derived glioma sphere lines (g157, g711, g1051 and g1079) with rhEndocan (10ng/ml)
319 for 3 days, followed by radiation treatment at 8 and 20 Gy. Analysis of these glioma spheres on
320 day 5 post-irradiation determined that rhEndocan pretreatment significantly enhanced cell
321 growth in three cell lines (**Figure 6B**), and decreased radiation-induced induction of caspase 3/7
322 activity assay even at radiation dose as high as 20 Gy (**Figures S5C, S5D)**. These effects were
323 at least partially attenuated by treatment of cells with a blocking antibody for endocan (**Figure**
324 **6C**).
325 We then created two tumor models by transplanting either WTD or KOD tumor cells into
326 WT brains, followed by treatment with an 8 Gy dose of radiation. Both tumor models showed
327 substantial shrinkage in size after radiation; nonetheless, the location of the resultant tumor cells
328 and the subsequent survival benefit were clearly different. Following radiation, residual KOD
329 tumor cells were scattered randomly around the injection sites, whereas post-radiation WTD
330 cells predominantly resided in the most distant areas in the corpus callosum - the "far-edge
331 area" and one of the most frequent brain regions with glioblastoma recurrence after treatment
332 failure [41, 42] . Subsequently, radiation showed a significantly greater effect on the survival of
333 tumor-bearing KO mice than in WT mice (**Figure 6D and 6E**). These data suggested that
334 endogenous endocan protects the tumor cells from radiation damage, thus promoting tumor
335 growth and diminishing animal survival.

336 Finally, we performed RNA-seq with glioma spheres that were treated with either HBEC-
337 5i CM or rhEndocan in presence of 8 Gy of radiation dose. Bioinformatics analysis
338 demonstrated that both HBEC-5i CM and endocan induce pronounced alterations in gene
339 expression, and importantly, addition of rhEndocan largely recapitulated the effects of HBEC-5i
340 CM on post-irradiation glioma spheres (**Figure 6F**). In fact, there was more than 70%
341 concordance of genes whose level of expression was altered more than 2-fold by both
342 treatments. These findings suggest that rhEndocan is one, if not the only, major mediator for the
343 VE cell-driven radioprotective effect on glioblastoma cells.
344
345

346 **Discussion**
347

348 Biological mechanisms of tumor evolution in primary glioblastoma cannot be directly
349 investigated in humans. With murine tumor models, this study uncovered that the cellular
350 hierarchy between two cell types that progress from a bi-potent edge+core-forming cell to core-
351 restricted mono-potent cells, no longer capable of producing cells capable of establishing
352 typical edge lesions. Unexpectedly, this cellular hierarchy is driven by a soluble factor from VE
353 cells, endocan. In the tumor microenvironment, this lineage-commitment occurs not only by
354 depletion of endocan (e.g. WTD cells in KO mice), but also loss of the ability to respond to
355 endocan, e.g. a receptor, in tumor cells (e.g. KOD cells in WT mice). We identified PDGFRα as
356 a critical receptor for endocan. Given the major roles of PDGFRα signaling in the propagation of
357 glioblastoma and other cancers, this data opens up new avenues of studying this endocan-
358 PDGFRα signaling axis [35, 43]. A critical question is how much of the effect of endocan on
359 tumor growth, radioprotection, and creation of the edge phenotype is due to the PDGFRα-
360 dependent signaling and how much is due to other mechanisms (**Illustration shown in Figure**
361 **7**). Our observations with ponatinib suggest that signaling through PDGFRα does play a

362 dominant role on endocan effect but does not exclude the possibility that endocan also acts
363 through undetermined PDGFRα-independent pathways. Given that hypovascular tumors in
364 *Esm1* KO mice would presumably retain PDGFBB or other PDGFs in the microenvironment,
365 endocan and PDGFs might drive sufficiently different downstream signaling cascades to create
366 different phenotypic outcomes. Another possibility is that PDGF ligand concentrations are
367 simply insufficient to fully activate the overlapping downstream signaling, subsequently causing
368 the less heterogeneous tumor phenotype.

369 Despite the striking phenotypic difference of the WTD and KOD tumors, the secondarily
370 generated core-located cells following endocan depletion were not solely a differentiated
371 progeny. It is reasonable to expect that the edge+core-generating ancestor-like cells should be
372 more malignant as opposed to the differentiated core-restricted progeny cells; nonetheless, the
373 survival of mice bearing WTD and KOD tumors are comparably similar. To our surprise, when
374 these two were combined, the resultant tumors displayed elevated malignancy, killing mice
375 faster than either alone. Of note, the WTD and co-injected tumors were phenotypically quite
376 similar, harboring both tumor edge and core. Collectively, these findings suggest that WTD and
377 KOD cells combine to extend the cellular heterogeneity in co-injected tumors, possibly through a
378 reflection of a cellular evolution mechanism. Taking the date this murine tumor model together,
379 we observed two sets of data that can only be explained by referring to both of two different
380 mechanisms: the cellular hierarchy theory (ancestor-like cells producing more fate-restricted
381 daughter cells) and the cellular evolution theory (two subtypes of tumor cells independently
382 contribute to tumor malignancy). From the therapeutic stand-point, our findings indicate that
383 surgery will need to eradicate the core cells completely, and that post-surgical adjuvant
384 therapies should then focus on the control of the edge cells toward achieving either elimination
385 or dormancy, preventing them from propagating and evolving into core lesions. Further studies
386 with multiple different preclinical models, possibly with patient-derived ones, are warranted.

387 Tumors are composed of two distinct subpopulations including the one that is located at
388 tumor edge, endocan-responsive, and more radioresistant [5]. Given the clinical challenges that
389 would be involved in the complete resection of edge-located tumor cells, the identification of
390 therapeutic targets associated with the tumor edge are an urgent need. Since a global KO of
391 *Esm1* does not cause noticeable defect in the brain or other organs, the idea of systemically
392 diminishing, or even completely eliminating, tumor-associated and/or radiotherapy-induced
393 endocan to control glioblastoma recurrence seems to be promising [26]. Furthermore,
394 endocan's vascular origin indicates that the blood brain barrier may not be a major roadblock to
395 the development of such therapeutics. However, single target approaches have failed for years
396 to control therapy-refractory cancers like glioblastoma. It is likely that future treatment strategy
397 would require the eradication of both endocan-responsive edge-located cells as well as their
398 endocan-independent core-located progeny as combination.
399
400
401 **ACKNOWLEDGEMENTS**
402 We would like to express our sincere appreciation to all the patients and families, who kindly
403 allowed us to obtain their tumor samples for this study. We thank Dr. Ralf Adams (Max Planck
404 Institute for Molecular Biomedicine) for generously sharing cryopreserved *Esm1* embryos. We
405 would also thank all our collaborating scientists, as well as the assigned reviewers and Editor for
406 this manuscript, for the constructive comments and suggestions. Lastly, we acknowledge the
407 contribution by all the members in the Nakano and Kornblum laboratories (past and present) for
408 technical assistance.
409
410
411

412 **FUNDING**

413 This work was supported by NIH grants R01NS083767, R01NS087913, R01CA183991,
414 R01CA201402 (I.N.), R01NS104339 (A.B.H), NS052563 (H.I.K.) the UCLA SPORE in Brain
415 Cancer, P50 CA211015 (H.I.K.); by the Russian Foundation for Basic Research grants 17-29-
416 06056 (M.S.P.), 17-00-00172 (K.S.A.), 20-04-00804 (M.S.P.) and 20-34-70147 (M.S.P.);
417 Russian Science Foundation grant 19-44-02027 (M.S.P.); grant 075-15-2019-1669 from the
418 Ministry of Science and Higher Education of the Russian Federation (K.S.A.) and the Dr. Miriam
419 and Sheldon G. Adelson Medical Research Foundation (H.I.K., A.L.B., S.A.G). D.N was
420 supported by the Korea Health Technology R&D Project through the Korea Health Industry
421 Development Institute (KHDI), funded by the Ministry of Health and Welfare, Republic of Korea
422 (HI4C3418).

423

424 **AUTHOR CONTRIBUTIONS**

425 Leading conceptualization: I.N; Critical rationalization: S.B, M.S.P, H.I.K, I.N; Methodology: S.B,
426 M.S.P, A.B.H, H.I.K, I.N; Laboratory investigation: S.B, M.S.P, Y.G, S.D.M, D.Y, M.S.K, J.A.O,
427 B.T, A.L.B, A.S, S.K.S; Bioinformatics analysis: H.J.C, Y.L, K.S.A, R.K, Y.C; Writing - Original
428 Draft: S.B, I.N; Writing – Review & Editing, S.B, M.S.P, H.I.K, I.N; Funding Acquisition: M.S.P,
429 K.S.A, A.B.H, H.I.K, A.L.B, S.A.G, I.N; Resources: H.I.K, A.L.B, I.N; Supervision: H.I.K, I.N.
430 All authors had substantial input to the logistics of the work and revised and approved the final
431 manuscript. The authors know their accountability for all aspects of the study ensuring that
432 questions regarding the accuracy and integrity of any part are appropriately investigated and
433 resolved. The corresponding authors had full access to all the data and the final responsibility to
434 submit the publication.

435

436 **DISCLOSURES**

437 The authors have nothing to disclose.

438 **METHODS**
439

440 **Informed consent and ethics committee approvals.** This study was conducted under
441 protocols approved by the IRBs and IACUCs of University of California Los Angeles (UCLA),
442 MD Anderson Cancer Center (MDA), and University of Alabama at Birmingham (UAB).

443 **The following experimental procedures were reported in our recent papers in detail [5,**
444 **11, 13].**

445 **Human Glioma sphere cell cultures**. As described previously, glioma sphere cultures were
446 maintained in DMEM/F12 medium supplemented with 2% B27 supplement (% vol), 20 ng/ml
447 bFGF, and 20 ng/ml EGF. The bFGF and EGF reagents were added twice a week, and the
448 culture medium was replaced every 7 days. Experiments with neurospheres were performed
449 with lines that were cultured for fewer than 30 passages since their initial establishment. STR
450 analysis was performed to confirm cell identity. The cell lines tested negative for mycoplasma
451 contamination.

452 **Human Tumor-Associated Endothelial Cell culture.** Glioblastoma tissues from patients were
453 freshly isolated during surgery, manually dissociated into single cells, and these cells were
454 sorted for CD31+ cells using magnetic beads (ThermoFisher Scientific). Following confirmation
455 of CD31 expression, VE cells were grown in fibronectin-coated flasks with 2% FBS, 1%
456 Penicillin-Streptomycin solution and 40μg/ml Endothelial growth supplement. Expression of
457 CD31 was periodically checked by flow cytometry.

458 **Murine Glioma sphere cell cultures.** Spontaneous tumors formed in *PTEN*, *TP53*, *NF1*
459 deleted mice [44] were grown in neurosphere media as described previously (mG7080).

460 **Freshly obtained mouse tumor in Fig 2A.** Freshly obtained mice tumor was kindly shared by
461 Dolores Hambardzyuman lab (Emory University). Tumor bearing hemisphere was visualized
462 and tumor was isolated to obtain single cells for injection into mice.

463 **HBEC-5i (ATCC)** cells: These cells were cultivated in DMEM/F12 medium containing 10% FBS,
464 1% Penicillin-Streptomycin solution and 40µg/ml Endothelial cell growth supplement.

465 **Genetically modified mice.** *Esm1* KO (Bl/6) mice are a generous gift from Dr. Ralf H.
466 Adams[26]. All animals were maintained in accordance with the National Institute of Health
467 (NIH) Guide for the care and Use of Laboratory Animals and were handled according to
468 protocols approved by the University of Alabama at Birmingham subcommittee on animal care
469 (Institutional Animal Care and Use Committee). Genomic status of *Esm1* was periodically
470 confirmed by PCR according to the prior studies [26].

471 **In Vivo Intracranial Xenograft Tumor Models**. As described previously, 6-8-week-old NOD
472 SCID mice ($Prkdc^{scid}$) were used for intracranial tumor formation. In each mouse, 5×10^5 cells of
473 human patient-derived glioblastoma cells were injected intracranially into groups of 6-8-week-
474 old mice. Detailed protocol is described elsewhere [13].

475 ***In Vivo* Syngeneic Intracranial Tumor Models.** Our general protocol for the intracranial tumor
476 models was described previously [13]. Briefly, 0.5 million murine glioblastoma cells were
477 injected into the brains of Bl/6 or *Esm1* KO mice as previously described [5]. Mice were
478 monitored and sacrificed when neuropathological symptoms developed. For
479 immunohistochemical studies, mice were perfused with ice-cold PBS, followed by 4%
480 paraformaldehyde (PFA). Mice brains were dissected and fixed in 4 % PFA solution for 48 hours
481 and then transferred to 10% formalin for 48 hours. For tumor collection for RNA extraction, mice
482 were sacrificed, and tumors were isolated and fast-frozen using liquid nitrogen.

483 ***In vivo* drug treatments.** Mice were injected with mg7080 tumors to form intracranial tumors.
484 On day 14 post injection, mice were treated with 50mg/kg/day of Ponatinib as recommended by
485 manufacturer's protocol (Selleckchem). Mice were administered ponatinib via oral gavage.

486 **Endocan enzyme-linked immunosorbent assay (ELISA).** The concentration of secreted
487 Endocan was measured using the Endocan ELISA kit (Boster Bio) according to the
488 manufacturer's protocol. Briefly, conditioned media was collected from the cells as mentioned
489 and used for the experimental study.

490 **Protein labeling.** Recombinant Endocan and PDGFBB were labeled with Alexa Fluor 488
491 Microscale Protein Labeling Kit and Alexa Fluor™ 647 Microscale Protein Labeling Kit
492 respectively. Labeled proteins were added to glioblastoma cells in different concentrations and
493 after 30 min incubation on ice, cells were washed twice with PBS and analyzed by Attune NxT
494 Flow Cytometer (Thermofisher Scientific). The obtained data were processed with FlowJo 10
495 software.

496 **Proximal Ligation Assay.** Glioblastoma cells were plated in wells of Lab-Tek II chamber pre-
497 coated with laminin and treated with Endocan or PDGFBB for 90 minutes. Next, cells were
498 washed 3 times with phosphate-buffered saline (PBS) and fixed with 4% PFA in PBS for 15 min
499 at room temperature. Cells were washed 2 times with PBS and permeabilized with 0.2% Triton-
500 X100 in PBS for 15 minutes. All subsequent procedures were performed using "Duolink In Situ
501 Orange Starter Kit" (Duolink) according to the manufacturer's protocol.
502

503 **Recombinant protein pull-down assay.** To obtain a protein complex, recombinant His-tagged
504 Endocan (R&D) was immobilized on 50 µl of HisPur Ni-NTA Magnetic Beads (Thermo Fisher
505 Scientific) according to the manufacturer's protocol. The beads were washed 3 times with PBS
506 and incubated for 2 hours with Fc-tagged recombinant PDGFRa (R&D) under constant

507 agitation. Next, beads were washed 3 times with PBS and bounded proteins were eluted with
508 300 mM imidazole in PBS and subjected to subsequent western blot analysis.

509 **Mass spectrometry.** Recombinant His-tagged Endocan (R&D) was immobilized on 50 µl of
510 HisPur Ni-NTA Magnetic Beads (Thermo Fisher Scientific) according to the manufacturer's
511 protocol. The beads were washed 3 times with PBS and incubated with fraction of plasma
512 membrane proteins that were isolated from g1079 cells as described previously[45] and
513 solubilized in lysis buffer (50 mM Tris-HCl, 150 mM NaCl, 1% Triton X100, 0.1% sodium
514 deoxycholate, protease inhibitor cocktail, pH 7.5). Next, beads were washed once with lysis
515 buffer and 3 times with PBS and bounded proteins were eluted with buffer containing 8M Urea,
516 2M Thiourea, 10 mM Tris (pH=8). Protein concentrations were determined using the QuickStart
517 Bradford protein assay (Bio-Rad) according to the manufacturer's protocol. Then protein
518 disulfide bonds were reduced with 5 mm DTT at RT for 30 min and afterward alkylated with 10
519 mm iodoacetamide at room temperature for 20 min in the dark. Detailed protocol can be found
520 in previous publication [13].

521 **In vitro migration experiment.** Glioma cells were cultured and dissociated into single spheres.
522 They were encapsulated with hydrogels as described in previous study [46].

523 **Exogenous Immunoprecipitation Assay.** Recombinant PDGFRα and Endocan (R&D) were
524 mixed together and incubated with pre-washed magnetic beads and volume was adjusted to
525 500 µL with Lysis Buffer and incubated with mixing under 4°C for 1 h to remove unspecific
526 bindings. The supernatant was collected with a magnetic stand and then incubated with the
527 antibody and mixed under 4°C overnight. Antigen sample/antibody mixture was transferred to
528 the tube and incubated with mixing under room temperature for 1 h. Magnetic beads were
529 collected with a magnetic stand and incubated with low-pH elution buffer at room temperature
530 with mixing for 10 min. The beads were magnetically separated and supernatant containing

531 target protein was saved. The pH was normalized with 15 µL of neutralization buffer for each
532 100 µL of elution buffer. IP samples were then loaded for electrophoresis with 4%-12% Bis-Tris
533 protein gel.

534 **Transmission Electron microscopy.** Tissue from tumor-bearing mice were resected after
535 anesthetizing, perfusing with 1X PBS. Tissue was immediately fixed in 2% glutaraldehyde at RT
536 (1 hour). The brains were then dehydrated in different concentrations of ethanol and 1% uranyl
537 acetate in 50% ethanol. Samples were then embedded and visualized using Tecnai Spirit T12
538 Transmission Electron Microscope.

539 **ATAC sequencing and analysis.** Previously-described methods [39] were used to perform
540 ATAC-sequencing. Briefly, 50,000 cells were washed with 50mL ice cold PBS and re-
541 suspended in 50mL lysis buffer (10 mM Tris-HCl pH 7.4, 10 mM NaCl, 3 mM MgCl2,0.2% (v/v)
542 IGEPAL CA-630). The suspension was centrifuged at 500g for 10 minutes at 4 degrees.
543 Samples were added with 50mL trans-position reaction mix of Nextera DNA library preparation
544 kit (FC-121-1031, Illumina). Samples were amplified by PCR and incubated at 37C for 30
545 minutes. MinElute Lit (Qiagen) was used to isolate DNA. NextSeq 500 High Output Kit v2 (150
546 cycle, FC-404-2002, Illumina) was used to sequence ATAC library. For analysis, alignment was
547 carried out using the Burrows-Wheeler Aligner mem, peak calling using MACS2 (with parameter
548 setting –nomodel –shift 75), GO enrichment analysis and peak annotation using HOMER.

549 **RNA sequencing.** cDNA were used in the library preparation using Ovation® Ultralow Library
550 Systems (NuGEN) and samples were sequenced using an Illumina HiSeq 2000 sequencer
551 (Illumina, San Diego, CA) in high output mode across 9 lanes of 50bppaired-end sequencing,
552 corresponding to 4.3 samples per lane and yielding between ~45 million reads per sample.
553 Additional QC was performed after the alignment to examine the level of mismatch rate,
554 mapping rate to the whole genome, repeats, chromosomes, key transcriptomic regions (exons,

555 introns, UTRs, genes), insert sizes, AT/GC dropout, transcript coverage and GC bias. Outliers
556 were removed based on QC results. Between 60 and 82% (avg 76%) of the reads were
557 mapped uniquely to the human genome. Total counts of read-fragments that were aligned to all
558 the candidate gene regions were derived using HTSeq program
559 (www.huber.embl.de/users/anders/HTSeq/doc/overview.html) with Human Hg38 (Dec.2014)
560 RefSeq (refFlat table) as a reference and used as a basis for the quantification of gene
561 expression. Only uniquely mapped reads were used for subsequent analyses. Differential
562 expression analysis was conducted with R-project and the Bioconductor package edgeR.
563 Statistical significance of the differential expression, expressed as Log_2 Fold Change (logFC),
564 was determined, using tag-wise dispersion estimation, at p-Value of <0.005 unless stated
565 otherwise. FPKM values were reported as a measure of relative expression units.

566 **Flow cytometry.** For CD44 staining glioma spheres were dissociated into single cells and
567 stained with anti-CD44-APC antibody (Miltenyi Biotec) according to manufacturer's protocol. For
568 CD133 staining, glioma spheres were dissociated into single cells and stained with anti-CD133-
569 FITC (Biolegend) according to manufacturer's protocol. For apoptosis assay, cells were stained
570 with CellEvent Caspase-3/7 Green Flow Cytometry Assay Kit (ThermoFisher Scientific)
571 according to the manufacturer's protocol. All samples were analyzed by Attune NxT Flow
572 Cytometer (Thermofisher Scientific) and the data were processed with FlowJo 10 software.

573 **Cell count assay.** AlamarBlue reagent (Thermo Scientific) was used to determine the cell
574 number under various treatments. Briefly, cells were seeded at a density of 5,000 cells per well
575 in 96-well plates. AlamarBlue reagent was added into each well and fluorescence was
576 measured (Excitation 515-565 nm, Emission 570-610 nm) using Synergy HTX multi-mode
577 reader (BioTek).

578 **Western blot.** The cell lysates were prepared in RIPA buffer containing 1% protease and 1%
579 phosphatase inhibitor cocktail on ice. The sample protein concentrations were determined using
580 the Bradford method. Equal amounts of protein lysates (10 μg/lane) were fractionated on a
581 NuPAGE Novex 4%–12% Bis-Tris Protein Gel (Thermo Fisher Scientific) and transferred onto a
582 PVDF membrane (Invitrogen, Thermo Fisher Scientific). Subsequently, the membranes were
583 blocked with 5% skim milk or 5% BSA for 1 hour and then treated with the appropriate antibody
584 at 4°C overnight. Protein expression was visualized with an Amersham ECL Western Blot
585 System (GE Healthcare Life Sciences). β-Actin served as a loading control. ImageJ software
586 (NIH) was used to analyze the Western blot results.

587 **Immunohistofluorescence.** Immunohistofluorescence (ICF) method was described previously
588 [5]. Briefly, tumors embedded in paraffin blocks were deparaffinized using Xylene and hydrated
589 through 100%, 95% and 75% ethanol gradient. Antigen was retrieved using DakoCytomation
590 target retrieval solution pH 6 (Dako). These samples were then blocked with serum-free protein
591 block solution (Dako) and incubated with corresponding primary antibodies at 4°C overnight.
592 Next, slides were incubated with Alexa Flour-conjugated secondary antibody for 1 hr at room
593 temperature and mounted in Vectashield mounting medium containing DAPI (Vector
594 Laboratories). Nikon A1 Confocal microscope (Nikon) was used to capture images.

595 **Immunohistochemistry.** Immunohistochemistry (IHC) method was described previously (Wang
596 et al., 2017). Briefly, tumors embedded in paraffin blocks were deparaffinized using Xylene and
597 hydrated through 100%, 95%, and 75% gradient of ethanol. Slides were then microwaved in the
598 presence of DakoCytomation target retrieval solution pH 6 (Dako). Slides were incubated with
599 0.3% hydrogen peroxide solution in methanol for 15 minutes at room temperature to inhibit
600 internal peroxide activity. Slides were then blocked with serum-free block solution (Dako) and
601 incubated with corresponding primary antibody overnight at 4°C. Next, samples were incubated

602 with EnVision+ System-HRP labeled Polymer (Dako) and visualized with DAB peroxidase
603 substrate kit (Vector Laboratories). IHC scoring was performed using a previously described
604 method (Klein et al., 2001). Samples with scores more than 4 were considered as "high"
605 expression group. Images were captured using Nikon EVOS® FL inverted microscope (Nikon).

606 **Lentivirus production and transduction.** 293FT (Invitrogen) cells were co-transfected with
607 vector encoding the GFP(Addgene) or mCherry (Addgene) using calcium phosphate (Clontech)
608 for lentivirus production. Lentivirus was harvested at 72 hr after transfection and concentrated
609 100-fold using Lenti-X concentrator (Clontech). Infection of lentivirus was performed according
610 to the manufacturer's protocol.

611 **Tissue Microarray.** Tissue microarray consisting of 0.6-mm cores from formalin-fixed, paraffin-
612 embedded tissue blocks were generated using patient derived glioblastoma tissue samples at
613 the Osaka City University.

614 **RNA Isolation and Quantitative Real-time PCR.** mRNA was extracted and purified using the
615 Qiagen RNeasy Mini kit according to the manufacturer's protocol. Nanodrop 2000
616 spectrophotometer was used to determine the concentration and quality of RNA. RNA (0.5-1μg)
617 was reverse-transcribed in cDNA using iScript reverse transcription supermix (Bio-Rad) that
618 was then amplified using the following cycling conditions. Cycling conditions were 95°C for 5
619 min, and then 50 cycles of 95°C for 30 s, 60°C for 30 s and 72°C for 30 s. qRTPCR was
620 performed on StepOnePlus thermal cycler (Thermo scientific) with SYBR Select Master Mix
621 (Thermo Scientific). 18s, Bactin or GAPDH were used as an internal control.

622 **Quantification and Statistical analysis.** All data are expressed as the mean ± SD. *P* values
623 were calculated in Graph Pad Prism 8.0 using a two-tailed Student t test which can be found in
624 the individual figures and figure legends. *P* values less than 0.05 were considered to be

625 significant. Log-rank analysis was used to determine the statistical significance of Kaplan-Meier
626 survival curves, and no samples, mice or data points were excluded from the analysis reported
627 in this study. Unless otherwise noted, statistical analysis was performed by Prism 6 (Graphpad
628 Software).
629
630 **Data availability.** All raw RNA-seq data will be available in the NCBI Gene Expression
631 Omnibus (prepared prior to publication).
632
633 **Reagent list.**

REAGENT or RESOURCE	SOURCE	IDENTIFIER
Antibodies		
Anti-ALDH1A3	Sigma-Aldrich	Cat# SAB1300933, RRID:AB_10607145
Anti-phospho AKT (Ser473)	Cell Signaling Technology	Cat# 9271, RRID:AB_329825
Anti-AKT	Cell Signaling Technology	Cat# 9272, RRID:AB_329827
Anti-β-ACTIN	Cell Signaling Technology	Cat# 2118; RRID:AB_561053
Anti-CD133-APC	Miltenyi Biotec	Cat# 130-090-826; RRID: AB_244340
Anti-CD31	Abcam	Cat# ab28364, RRID:AB_726362
Anti-CD31	Novus	Cat#NB600-562, RRID:AB_10002476
Anti-CD44	Cell Signaling Technology	Cat# 3578; RRID: AB_2076463
Anti-CD44-FITC	BioLegend	Cat# 338804, RRID:AB_1501197
Endocan blocking antibody	R&D systems	Cat# AF1810-SP
Anti-ESM1	Abcam	Cat# ab56914, RRID:AB_941479
Anti-ESM1	Bioss	Cat# bs-3615R, RRID:AB_10857499
GAPDH	Abcam	Cat# ab9483; RRID: AB_307273
Anti-Goat IgG control	Thermofisher Scientific	**Catalog #** 02-6202
Anti-GFP	Abcam	Cat# ab290; RRID:AB_303395
Anti-phospho GSK3β (Thr 390)	Bioss	Cat# bs-3148R, RRID:AB_10857056
Anti-GSK3β	Cell Signaling Technology	Cat# 12456, RRID:AB_2636978
Anti-HIF1α	Novus	Cat# NB100-105, RRID:AB_10001154
Anti-His-tag	Cell Signaling Technology	Cat# 12698, RRID:AB_2744546
Rabbit IgG Isotype Control	Thermofisher Scientific	Cat# 02-6102, RRID:AB_2532938
Anti-phospho-p44/42 MAPK	Cell Signaling Technology	Cat# 9101, RRID:AB_331646
Anti-p44/42 MAPK	Cell Signaling Technology	Cat# 9102, RRID:AB_330744

Anti-mCHERRY	Novus	Cat# NBP2-25157, RRID:AB_2753204
Anti-MYC	Santa Cruz Biotechnology	Cat# SC-40; RRID: AB_627268
Anti-p65-NF-κB(pS536)	Abcam	Cat# ab86299, RRID:AB_1925243
Anti-OLIG2	Millipore	Cat# AB9610; RRID: AB_570666
Anti-PI3K p85 / p55, phospho (Tyr199)	Bioworld Technology	Cat# BS4605, RRID: AB_1663852
Anti-PI3K	Cell Signaling Technology	Cat# 4292, RRID:AB_329869
Anti-phospho PDGFRα (y720)	Abcam	Cat# ab134068
Anti-PDGFRα	Cell Signaling Technology	Cat# 3174, RRID:AB_2162345
Anti-PDGFRα (C-terminal)	Sigma-Aldrich	Cat# SAB1404186, RRID:AB_10737660
Bacterial and Virus Strains		
E. coli Stbl3 Competent cells	ThermoFisher	Cat# C737303
Biological Samples		
Human glioma tissue microarray	This study	N/A
Human glioma tissues	This study	N/A
Human blood plasma samples	This study	N/A
Mouse tissues	This study	N/A
Chemicals, Peptides, and Recombinant Proteins		
EGF	Peprotech	Cat# AF-100-15
bFGF	Peprotech	Cat# AF-100-18B
B27	Thermofisher	Cat# 12587010
Heparin	Sigma	Cat# H3149
DMEM/F12	Thermofisher	Cat# 10565-018
StemPro Accutase	Thermofisher	Cat# A1110501
Fetal bovine serum	Thermofisher	Cat# 10438018
Penicillin-Streptomycin	Thermofisher	Cat# 15140122
Laminin	Sigma	Cat# 11243217001
Endothelial cell growth supplement	Sigma	Cat# E2759
RIPA buffer	Sigma	Cat# R0278
Phosphatase inhibitor cocktail	Sigma	Cat# P2850
Protease inhibitor cocktail	Sigma	Cat# P8340
Blotting Grade Blocker Non Fat Dry Milk	Bio-Rad	Cat# 1706404XTU
iScript reverse transcription supermix	Bio-Rad	Cat# 1708841
SYBR select master mix	Thermofisher	Cat# 4472918
Serum-free protein block solution	Dako	Cat# X090930-2
Vectashield mounting medium containing DAPI	Dako	Cat# H-1200
DakoCytomation target retrieval solution pH6	Dako	Cat# S236984-2

Envision+ System-HRP labeled Polymer	Dako	Cat# K400211-2
AlamarBlue reagent	ThermoFisher	Cat# DAL1100
Alexa-Fluor 488 5-TFP Ester	ThermoFisher	Cat# A30005
Polybrene	EMD Millipore	Cat# TR-1003-G
Puromycin	Sigma	Cat# P7255
Recombinant Endocan	R&D	Cat#
Recombinant PDGFBB	R&D	
Alexa-Fluor 647 microscale protein kit	Thermofisher	Cat# A30009
Duolink Insitu Orange Starter Kit	Duolink	Cat# DUO92102
HisPur Ni-NTA Magnetic Beads	Thermofisher	Cat# 88831
F_c Tagged recombinant PDGFRα		Cat# 6765-PR-050
Critical Commercial Assays		
Dual reporter luciferase assay	Promega	Cat# E1910
HiSpeed Plasmid Midi RNeasy mini kit	Qiagen	Cat# 12643
Kit miRNeasy mini kit	Qiagen	Cat# 217004
Qiagen Cat# 74104 DAB peroxidase substrate kit	Vector Laboratories	Cat# SK-4100
CellEvent Caspase-3/7 Green Flow Cytometry Assay Kit	ThermoFisher	Cat# C10427
Autophagy Detection Kit	Abcam	Cat# ab139484
Quick Start Bradford protein assay	Bio-Rad	Cat# 5000201
TruSeq Stranded mRNA-Seq Library Preparation Kit	Illumina	Cat# 20020594
ESM1 ELISA KIT	BosterBio	Cat# EK0752
Ponatinib	Selleckchem	Cat# S1490
Deposited Data		
RNA sequencing data	This study	GEO accession# GSE137809
RNA sequencing data expression	This study	Table S1
ATAC-seq data	This study	GEO accession# GSE137809
ATAC sequencing data expression	This study	Table S2, S3
Experimental Models: Cell Lines		
Normal Human Astrocytes	Lonza	Cat# CC-2565
HBEC-5i	ATCC	Cat# CRL-3245
hG157	Mao et al., 2013[47][47][46][45][44][45][44][44][44][44][44][44][43]	See Table S4
hG711	(Bhat et al., 2013)	See Table S4

hG1051	(Minata et al., 2019)	See Table S4
hG1079	(Minata et al., 2019)	See Table S4
TEC15	This study	See Table S4
293FT	Thermofisher	Cat#R70007
mG7080	(Sadahiro et al., 2018)	N/A
PDGFBB1	This study	N/A
Experimental Models: Organisms/Strains		
NOD scid mice -Prkdc^{scid}	The Jackson Laboratory	Cat# 001303
C57BL6	The Jackson Laboratory	Cat# 000664
ESM1 knockout mice	(Rocha et al., 2014)	N/A
Oligonucleotides		
Primers for qRT-PCR	This study	See Methods section
Recombinant DNA		
psPAX2	Addgene	Cat# 12260
GFP	Addgene	N/A
mCherry	Addgene	N/A
pMD2.G	Addgene	Cat# 12259
Software and Algorithms		
GraphPad Prism	GraphPad Software N/A	N/A
FlowJo 10	FLOWJO, LLC	N/A
ImageJ	NIH	N/A
Ingenuity Pathway Analysis	Qiagen	N/A

634 Supplemental Table S5: Oligonucleotides

Species	Sequences
Human 18S	Forward: GGCCCTGTAATTGGAATGAGTC Reverse: CCAAGATCCAACTACGAGCTT
Human ESM1	Forward: TCCCGGCTGTGATTTCTGAG Reverse: ACCATGCATCACATTTGGTCTTC
Human NFκB:	Forward: CCT GGA TGA CTC TTG GGA AA Reverse: TCA GCC AGC TGT TTC ATG TC
Human PDGFRα	Forward: AGGGATAGCTTCCTGAGCCA

	Reverse: AGCTCCGTGTGCTTTCATCA
Human Bactin	Forward: AGAAGAGCTATGAGCTGCCTGACG Reverse: TACTTGCGCTCAGGAGGAGCAATG
Human GAPDH	Forward: GAA GGT GAA GGT CGG AGT CA Reverse: TTG AGG TCA ATG AAG GGG TC
Mouse Podocalyxin	Forward: TACTGTCGCCTGCATCTCAC Reverse: TGATGTTGTGGCACTTTGGT
Mouse SMa	Forward: AGACAGCTATGTGGGGGATG Reverse: CTTTTCCATGTCGTCCCAGT
Mouse Occludin	Forward: GCGGAAAGAGTTGACAGTCC Reverse: GGCACCAGAGGTGTTGACTT
Mouse CD31	Forward: GCCCAATCACGTTTCAGTTT Reverse: AAAACGCTTGGGTGTCATTC
Mouse Claudin5	Forward: AAATTCTGGGTCTGGTGCTG Reverse: GTCACGATGTTGTGGTCCAGM
Mouse PEDF	Forward: ACCGTGACCCAGAACTTGAC Reverse: GACAGTCAGCACAGCTTGGA
Mouse GAPDH	Forward: GTT GTC TCC TGC GAC TTC Reverse: GGT GGT CCA GGG TTT CTT

Mouse VWF	Forward: CAGCATCTCTGTGGTCCTGA Reverse: GGAGGCTGCTAGTGGTGAAG

654 **REFERENCES**

655 1. Kuhnt, D., et al., *Correlation of the extent of tumor volume resection and patient survival in surgery of*
656 *glioblastoma multiforme with high-field intraoperative MRI guidance.* Neuro-Oncology, 2011. **13**(12): p.
657 1339-1348.
658 2. Sottoriva, A., et al., *Intratumor heterogeneity in human glioblastoma reflects cancer evolutionary dynamics.*
659 Proc Natl Acad Sci U S A, 2013. **110**(10): p. 4009-14.
660 3. Brennan, C.W., et al., *The somatic genomic landscape of glioblastoma.* Cell, 2013. **155**(2): p. 462-77.
661 4. Li, C., et al., *Tumor Edge-to-Core Transition Promotes Malignancy in Primary-to-Recurrent Glioblastoma*
662 *Progression in a PLAGL1/CD109-mediated mechanism.* bioRxiv, 2020: p. 2020.09.14.293753.
663 5. Bastola, S., et al., *Glioma-initiating cells at tumor edge gain signals from tumor core cells to promote their*
664 *malignancy.* Nat Commun, 2020. **11**(1): p. 4660.
665 6. Spiteri, I., et al., *Evolutionary dynamics of residual disease in human glioblastoma.* Ann Oncol, 2019. **30**(3):
666 p. 456-463.
667 7. Minata, M., et al., *Phenotypic Plasticity of Invasive Edge Glioma Stem-like Cells in Response to Ionizing*
668 *Radiation.* Cell Rep, 2019. **26**(7): p. 1893-1905 e7.
669 8. Jin, X., et al., *Targeting glioma stem cells through combined BMI1 and EZH2 inhibition.* Nature Medicine,
670 2017. **23**(11): p. 1352-1361.
671 9. Lasocki, A. and F. Gaillard, *Non-Contrast-Enhancing Tumor: A New Frontier in Glioblastoma Research.*
672 American Journal of Neuroradiology, 2019.
673 10. Yan, J.-L., et al., *Multimodal MRI characteristics of the glioblastoma infiltration beyond contrast*
674 *enhancement.* Therapeutic advances in neurological disorders, 2019. **12**: p. 1756286419844664-
675 1756286419844664.
676 11. Yamashita, D., et al., *Targeting glioma-initiating cells via the tyrosine metabolic pathway.* J Neurosurg,
677 2020: p. 1-12.
678 12. Ibrahim, A.N., et al., *Intratumoral spatial heterogeneity of BTK kinomic activity dictates distinct therapeutic*
679 *response within a single glioblastoma tumor.* J Neurosurg, 2019: p. 1-12.
680 13. Pavlyukov, M.S., et al., *Apoptotic Cell-Derived Extracellular Vesicles Promote Malignancy of Glioblastoma*
681 *Via Intercellular Transfer of Splicing Factors.* Cancer Cell, 2018. **34**(1): p. 119-135 e10.
682 14. Holash, J., et al., *Vessel cooption, regression, and growth in tumors mediated by angiopoietins and VEGF.*
683 Science, 1999. **284**(5422): p. 1994-8.
684 15. Hambardzumyan, D. and G. Bergers, *Glioblastoma: Defining Tumor Niches.* Trends Cancer, 2015. **1**(4): p.
685 252-265.
686 16. Calabrese, C., et al., *A perivascular niche for brain tumor stem cells.* Cancer Cell, 2007. **11**(1): p. 69-82.
687 17. Charles, N., et al., *Perivascular nitric oxide activates notch signaling and promotes stem-like character in*
688 *PDGF-induced glioma cells.* Cell Stem Cell, 2010. **6**(2): p. 141-52.
689 18. Christensen, K., H.D. Schroder, and B.W. Kristensen, *CD133+ niches and single cells in glioblastoma have*
690 *different phenotypes.* J Neurooncol, 2011. **104**(1): p. 129-43.
691 19. Christensen, K., H.D. Schroder, and B.W. Kristensen, *CD133 identifies perivascular niches in grade II-IV*
692 *astrocytomas.* J Neurooncol, 2008. **90**(2): p. 157-70.
693 20. Burgett, M.E., et al., *Direct contact with perivascular tumor cells enhances integrin alphavbeta3 signaling*
694 *and migration of endothelial cells.* Oncotarget, 2016. **7**(28): p. 43852-43867.
695 21. Lassalle, P., et al., *ESM-1 is a novel human endothelial cell-specific molecule expressed in lung and regulated*
696 *by cytokines.* J Biol Chem, 1996. **271**(34): p. 20458-64.
697 22. Kali, A. and K.S. Shetty, *Endocan: a novel circulating proteoglycan.* Indian J Pharmacol, 2014. **46**(6): p.
698 579-83.
699 23. Scherpereel, A., et al., *Overexpression of endocan induces tumor formation.* Cancer Res, 2003. **63**(18): p.
700 6084-9.
701 24. Maurage, C.A., et al., *Endocan expression and localization in human glioblastomas.* J Neuropathol Exp
702 Neurol, 2009. **68**(6): p. 633-41.
703 25. Almog, N., et al., *Transcriptional switch of dormant tumors to fast-growing angiogenic phenotype.* Cancer
704 Res, 2009. **69**(3): p. 836-44.

705 26. Rocha, S.F., et al., *Esm1 modulates endothelial tip cell behavior and vascular permeability by enhancing*
706 *VEGF bioavailability.* Circ Res, 2014. **115**(6): p. 581-90.
707 27. Herting, C.J., et al., *Tumour-associated macrophage-derived interleukin-1 mediates glioblastoma-associated*
708 *cerebral oedema.* Brain, 2019. **142**(12): p. 3834-3851.
709 28. Zhu, Y., et al., *Early inactivation of p53 tumor suppressor gene cooperating with NF1 loss induces malignant*
710 *astrocytoma.* Cancer Cell, 2005. **8**(2): p. 119-30.
711 29. Hemmati, H.D., et al., *Cancerous stem cells can arise from pediatric brain tumors.* Proceedings of the
712 National Academy of Sciences, 2003. **100**(25): p. 15178-15183.
713 30. Laks, D.R., et al., *Neurosphere formation is an independent predictor of clinical outcome in malignant*
714 *glioma.* Stem Cells, 2009. **27**(4): p. 980-7.
715 31. Heldin, C.H. and B. Westermark, *Mechanism of action and in vivo role of platelet-derived growth factor.*
716 Physiological Reviews, 1999. **79**(4): p. 1283-1316.
717 32. Heldin, C.H., A. Ostman, and L. Rönnstrand, *Signal transduction via platelet-derived growth factor*
718 *receptors.* Biochim Biophys Acta, 1998. **1378**(1): p. F79-113.
719 33. Hermanson, M., et al., *Platelet-derived growth factor and its receptors in human glioma tissue: expression*
720 *of messenger RNA and protein suggests the presence of autocrine and paracrine loops.* Cancer Res, 1992.
721 **52**(11): p. 3213-9.
722 34. Betsholtz, C., *Biology of platelet-derived growth factors in development.* Birth Defects Res C Embryo Today,
723 2003. **69**(4): p. 272-85.
724 35. Ozawa, T., et al., *PDGFRA gene rearrangements are frequent genetic events in PDGFRA-amplified*
725 *glioblastomas.* Genes Dev, 2010. **24**(19): p. 2205-18.
726 36. Martinho, O., et al., *Expression, mutation and copy number analysis of platelet-derived growth factor*
727 *receptor A (PDGFRA) and its ligand PDGFA in gliomas.* Br J Cancer, 2009. **101**(6): p. 973-82.
728 37. Jackson, E.L., et al., *PDGFR alpha-positive B cells are neural stem cells in the adult SVZ that form glioma-*
729 *like growths in response to increased PDGF signaling.* Neuron, 2006. **51**(2): p. 187-99.
730 38. Roskoski, R., Jr., *The role of small molecule platelet-derived growth factor receptor (PDGFR) inhibitors in*
731 *the treatment of neoplastic disorders.* Pharmacol Res, 2018. **129**: p. 65-83.
732 39. Buenrostro, J.D., et al., *ATAC-seq: A Method for Assaying Chromatin Accessibility Genome-Wide.* Curr
733 Protoc Mol Biol, 2015. **109**: p. 21 29 1-9.
734 40. Cavallin, L.E., et al., *KSHV-induced ligand mediated activation of PDGF receptor-alpha drives Kaposi's*
735 *sarcomagenesis.* PLOS Pathogens, 2018. **14**(7): p. e1007175.
736 41. Tamura, R., et al., *Visualization of spatiotemporal dynamics of human glioma stem cell invasion.* Molecular
737 Brain, 2019. **12**(1): p. 45.
738 42. de Groot, J.F., et al., *Tumor invasion after treatment of glioblastoma with bevacizumab: radiographic and*
739 *pathologic correlation in humans and mice.* Neuro Oncol, 2010. **12**(3): p. 233-42.
740 43. Neftel, C., et al., *An Integrative Model of Cellular States, Plasticity, and Genetics for Glioblastoma.* Cell,
741 2019. **178**(4): p. 835-849.e21.
742 44. Alcantara Llaguno, S., et al., *Malignant Astrocytomas Originate from Neural Stem/Progenitor Cells in a*
743 *Somatic Tumor Suppressor Mouse Model.* Cancer Cell, 2009. **15**(1): p. 45-56.
744 45. Gotlib, L.J. and D.B. Searls, *Plasma membrane isolation on DEAE-Sephadex beads.* Biochim Biophys Acta,
745 1980. **602**(1): p. 207-12.
746 46. Xiao, W., et al., *Hyaluronic-Acid Based Hydrogels for 3-Dimensional Culture of Patient-Derived*
747 *Glioblastoma Cells.* J Vis Exp, 2018(138).
748 47. Mao, P., et al., *Mesenchymal glioma stem cells are maintained by activated glycolytic metabolism involving*
749 *aldehyde dehydrogenase 1A3.* Proceedings of the National Academy of Sciences of the United States of
750 America, 2013. **110**(21): p. 8644-8649.
751

752

753

754 **Figure Legends**

755

756 **Figure 1. Tumor-associated VE cells promote glioblastoma aggressiveness in vivo,**

757 **accompanied by their secretion of endocan**

758 (A) Pre-operation MRI T1-weighted, and perfusion Magnetic Resonance imaging (MRI) of a

759 glioblastoma patient highlighting necrotic core (enhancing on T1, blue intensity on perfusion)

760 and vasculature-rich edge (enhancing on T2, green intensity on perfusion) areas.

761 (B) Kaplan-Meier survival analysis of SCID mice following intracranial injection of glioma

762 spheres (hG1051) or glioma spheres (hG1051) +Tumor Endothelial cells (TEC15) at 1:10 ratio.

763 ***P=0.003, log-rank test (n=5 mice per group).

764 (C) Schematic outlining the screening procedure to identify paracrine signals of VE cells from 8

765 glioblastoma patient samples.

766 (D) Volcano plot of RNA-sequencing (RNA-seq) data comparing gene expressions of normal

767 and tumor endothelial cells, with Es(red arrow). FC=9.76, FDR-corrected p-value=0.0031.

768 (E)TCGA LGG and HGG cohort to compare expression of endocan in TCGA's WHO grade II,

769 III, and IV tumors.

770 (F) Depiction of SMC cohort data set showing the level of endocan expression in grade IV

771 Glioma.

772 (G) Kaplan-Meier analysis showing the correlation between endocan expression and the

773 survival of 667 glioma patients. P = 0.044, by log-rank test.

774 (H) ELISA comparing levels of secreted endocan in CM from NHA, HBEC-5i, g157, g711 and

775 g1051. *P=0.0001; two-tailed Student's t-test. Scale bar, 50 μm. All quantitative data are

776 average ±SD; *P<0.01, **P<0.001, ***P<0.0001.

777 (I) Representative immunofluorescence (IF) staining of endocan or CD31 in formalin-fixed
778 paraffin-embedded tissue sections from glioblastoma patient hG1051. Nuclei stained with DAPI.
779 Scale bar, 50 μm. All quantitative data are average ±SD; *P<0.01, **P<0.001, ***P<0.0001.
780

781 **Figure 2. Endocan is required for establishing the hypervascular tumor edge structure in**
782 **murine glioblastoma**

783 (A) Murine glioblastoma tissues collected from tumor formed in Nestin-Tva/Cdkn2a-/- mice
784 formed by RCAS-PDGFB injection. Tumor was obtained, sliced into single cells and injected
785 into WT or *Esm1* KO mice, gross images from WT and KO mice brains (upper). H&E (middle).
786 (B) CD31 staining (lower) of WTD or *Esm1* KOD tumor and non-tumor bearing brain
787 hemispheres. Scale bar, 200 μm.
788 (C) mg7080 murine glioblastoma cells formed in *PTEN/P53/NF1* deleted glioblastoma model.
789 Tumor was obtained and cells were put in culture in neurosphere medium. Gross images
790 depicting brains collected form mG7080 glioma-bearing *Esm1* KO or WT mice (upper). H&E
791 (middle).
792 (D) CD31 staining (lower) of mG7080 *Esm1* KOD or WTD tumor and non-tumor bearing brain
793 hemispheres. Scale bar, 200 μm.
794 (E) Transmission electron microscopy (TEM) of WTD and *Esm1* KOD normal and tumor tissues.
795 The following structures are indicated in imaging: Endothelial cell (EC). Scale bar, 500 nm.
796

797 **Figure 3. Endocan-driven edge+core and endocan-depleted core lesions cooperatively**
798 **increase intratumoral heterogeneity, elevating the malignancy of murine glioblastoma**

799 (A) Schematic outlining injection of mg7080 spheres in WT and *Esm1* KO host, followed by
800 isolation of tumor cells, labeling *Esm1* KO derived spheres with mCherry and WT derived
801 spheres with GFP and co-injection into WT host.

802 (B) IHC staining for GFP and mCherry positive cells in co-injected WT host brain indicating the
803 migration pattern of tumor cells. Injection site indicated by *.
804 (C) IHC staining for the VE marker (CD31), and hypovascularity markers (HIF1α, ALDH1A3,
805 and YKL-40) in co-injected *Esm1* WT-GFP + KO-mCherry mice brain tumors comparing core
806 (upper) and edge (lower) areas (n=5 mice per group).
807 (D) DAB intensity analysis scoring for respective tumor edge and core areas (lower). Scale bar,
808 200 μm. *t*-test, ***P*<0.01, ****P*<0.001; n=6; s.d. (error bar).
809 (E) IHC staining for GFP and mCherry positive cells in co-injected *Esm1* KO host brain
810 indicating the migration pattern of tumor cells. Injection site indicated by *.
811 (F, G) Kaplan-Meier survival analysis for WT or *Esm1* -/-mice following intracranial injection of
812 *Esm1* KO-mCherry, WT-GFP or both (mix) at 1:1 ratio. (n=5 mice per group), **P*=0.047; by
813 comparing 1:1 mix and WT. ns *P*=0.31; by comparing WT and *Esm1* KO. ***P*=0.00642; by
814 comparing 1:1 mix and *Esm1* KO. *P*-values were determined by log-rank test. All quantitative
815 data are average ±SD; **P*<0.01, ***P*<0.001, ****P*<0.0001, two-tailed Student's *t*-test.
816
817 **Figure 4. Endocan binds to and phosphorylates PDGFRα in human glioblastoma cells**
818 (A) Schematic outlining identification of PDGFRα as a receptor of Endocan via rhEndocan
819 knockdown of hG157 cells followed by mass spectrometry.
820 (B) Immunoprecipitation (IP) Western blot (WB) demonstrating binding of exogenous His-tagged
821 rhEndocan and Fc-tagged rhPDGFRα.
822 (C) Graphical comparison of endocan binding intensities following administration of 0-10 ug/ml
823 PDGFBB or endocan to hG1079 cells
824 (D) Adjacent slide IHCs for endocan (left) and PDGFRα (right) of glioblastoma patient 101027
825 tumor samples.

826 (E) WB comparing phosphorylation of PDGFRα (Y720) following the addition of 10ng/ml
827 rhEndocan or rhPDGFBB, measured at distinct time-points. WB comparing phosphorylation of
828 downstream targets of PDGFRα (Y720) following the addition of 10ng/ml rhEndocan or
829 rhPDGFBB, measured at distinct time-points.
830 (F) WB comparing phosphorylation of downstream PDGFRα targets following the addition of
831 10ng/ml of rhEndocan or rhPDGFBB, measured at distinct time-points.
832 (G) Kaplan Meier survival analysis of Bl/6 mice following intracranial injection of WT-GFP and
833 KO-mCherry cells. Mice were treated with 50mg/kg/day dose of ponatinib for 5 days, compared
834 to control. *P<0.046. P-value was determined by log-rank test.
835 (H) IHC staining of tumor-bearing mice brains following intracranial for mCherry, PDGFRα,
836 Olig2, pP65-NF-κB in control (upper), Ponatinib treated group (lower). Mice were treated with
837 50mg/kg/day compared to control. DAB intensity analysis scoring for respective tumors (lower).
838 t-test, ***P<0.001; n=5; s.d. (error bar). All quantitative data are average ±SD; *P<0.01,
839 **P<0.001, ***P<0.0001, two-tailed Student's t-test.
840
841 **Figure 5. Endocan-mediated signaling alters chromatin accessibility in glioblastoma**
842 **cells, including the promoter region of the Myc gene**
843 (A) ATAC-seq analysis for WTD and *Esm1* KOD tumors shows changes in WTD vs. KOD
844 tumors (n=2 mice per group).
845 (B) ATAC-seq and RNA-seq analysis for the Myc gene from WTD and *Esm1* KOD tumors.
846 (C) MYC gene is implicated in *Esm1* KOD tumors (shown by red arrow) in RNA-seq data.
847 (D) IHC analysis for WTD and *Esm1* KOD tumors for MYC expression.
848 (E) Schema highlighting the edge like phenotype conferred by endocan.
849

850 **Figure 6. Endocan protects edge-located glioblastoma cells from radiotherapy-induced**
851 **cell death *in vivo***
852 (A) ELISA for secreted endocan from HBEC-5i cells in CM following irradiation with 8 Gy at 1, 2,
853 3 time-points. ****P<0.0001, 2-tailed t-test.
854 (B) *In vitro* radio-sensitivity assay for glioma spheres (g157, g711, g267, g1079) pretreated with
855 rhEndocan for 3 days and irradiated on Day 3. Cell growth was measured on Day 7. **P<0.01,
856 ***P<0.001, 2-tailed t-test.
857 (C) Alamar Blue to measure the cell growth post radiation for Control, IgG and endocan blocking
858 in HBEC-5i CM. ***P<0.001, ****P<0.0001, 2-tailed t-test. (D) H&E of *Esm1* WTD (upper) or
859 KOD (lower) mice brains following intracranial injection of mG7080 cells and administration of
860 2.5 Gy irradiation for 3 days. Mice were sacrificed 2 weeks post-radiotherapy. Mice brain slices
861 were compared to sham-irradiated mice. n=5 mice.
862 (E)Kaplan Meier survival analysis of *Esm1* WT or *Esm1* -/- mice following intracranial injection
863 of mG7080 cells. Mice were radiated with 2.5 Gy for 3 days and were monitored for tumor
864 burden. P-value was determined by log-rank test.
865 (F) Gene-set enrichment analysis using Gene Ontology database comparing genes upregulated
866 and downregulated after treatment with endocan and VE CM (2-fold or higher). All quantitative
867 data are average ±SD; *P<0.01, **P<0.001, ***P<0.0001.
868

869 **Supplementary Figure Legends**

870 **Supplementary Figure 1: related to Figure 1**
871 (A)Pre-operation and post-operation MRI T1-weighted, and perfusion Magnetic Resonance
872 imaging (MRI) of a glioblastoma patient highlighting necrotic core (enhancing on T1, blue
873 intensity on perfusion) and vasculature-rich edge (enhancing on T2, green intensity on
874 perfusion) areas.

875

876 **Supplementary Figure 2: related to Figure 1**

877 (A) MRI T1-weighted, and perfusion Magnetic Resonance imaging (MRI) of a glioblastoma
878 patient highlighting necrotic core (enhancing on T1, blue intensity on perfusion) and
879 vasculature-rich edge (enhancing on T2, green intensity on perfusion) areas. Microscopic intra-
880 operative view highlights edge and core areas (edge indicated by white line and arrows, core
881 indicated by yellow line and arrow).

882 (B)Schema showing isolation of patient derived vascular endothelial cells.

883 (C) Kaplan-Meier survival analysis of SCID mice following intracranial injection of g1051 or
884 g1051+HBEC-5i cells at 1:10 ratio. ***P=0.003, log-rank test (n=5 mice per group) ***P <0.001,
885 by log-rank test.(D) Representative immunohistochemistry (IHC) staining of CD31(red) in mice
886 glioblastoma tumors formed in control (upper) or hG1051+TEC15 co-injection (lower) groups.
887 (n=5 mice per group). Scale bar, 100 μm.

888

889 **Supplementary Figure 3: related to Figure 2**

890 (A)Normal H&E and CD31 staining in non-tumor section in these two tumor models.

891 (B) Representative images of g1005 and g1037 spheres with and without endocan under the *in*
892 *vitro* migration-inducing condition when they were encapsulated in hydrogels.

893

894 **Supplementary Figure 4: related to Figure 4**

895 (A) Box plot showing PLA signals of PDGFRα or rhEndocan, rhPDGFBB, and control group.
896 hG1051 cells were used. 2-tailed *t*-test, *P<0.05, ***P<0.001. s.d. (error bar).

897 (B) Graphical comparison of endocan and PDGFBB binding intensities following administration
898 of 0-10 ug/ml PDGFBB or endocan to hG1079 cells.

899 (C) GSEA for comparisons of RNA-seq data from tumors in WTD and KOD mice (A) to gene
900 sets representing angiogenesis genes.
901 (D) qRT-PCR for vascular associated genes in tumors from WTD and KOD mice. All
902 quantitative data are average ±SD; *P<0.01, **P<0.001, ***P<0.0001, two-tailed Student's t-test.
903
904 **Supplementary Figure 5: related to Figure 5**
905 (A) qRT-PCR for *ESM1* from HBEC-5i cells treated with 50μM TMZ treatment 24 and 48 hrs
906 after treatment.
907 (B) qRT-PCR measurement of *ESM1* transcripts from HBEC-5i cells following 8Gy irradiation at
908 24 and 48 hr. ****P<0.0001, 2-tailed t-test.
909 (C, D) Flow cytometry analysis of caspase 3/7 activity and SYTOX staining of hG1079 cells
910 pretreated with rhEndocan and HBEC-5i CM for 3 days, irradiating it on Day 3 and staining on
911 Day 7. All quantitative data are average ±SD; *P<0.01, **P<0.001, ***P<0.0001, two-tailed
912 Student's t-test.

Figure 1

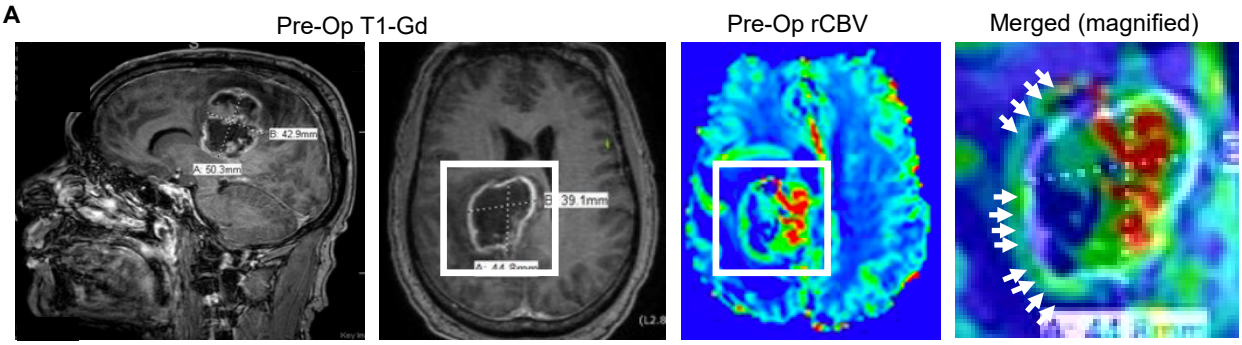
A
Pre-Op T1-Gd
Pre-Op rCBV
Merged (magnified)
B 42.9mm
A 50.3mm
B 39.1mm

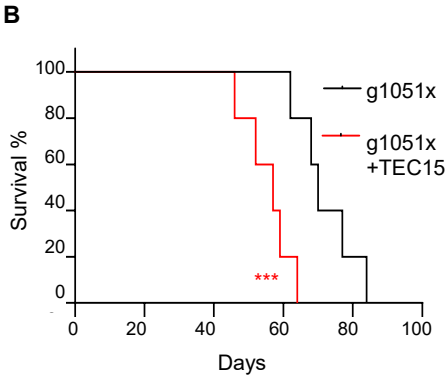
B
Survival %
Days
g1051x
g1051x
+TEC15
***

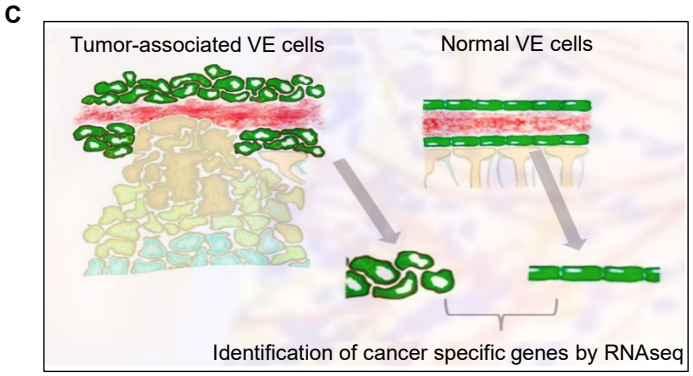
C
Tumor-associated VE cells
Normal VE cells
Identification of cancer specific genes by RNAseq

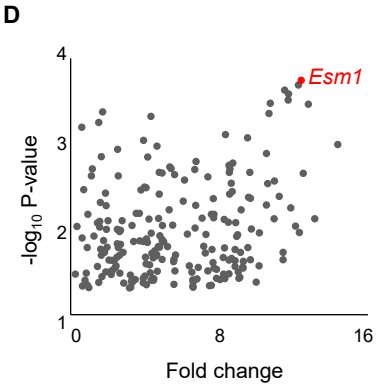
D
Esm1
-log10 P-value
Fold change

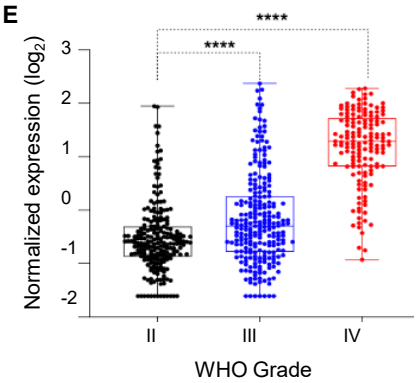
E
****
****
Normalized expression (log2)
WHO Grade
II
III
IV

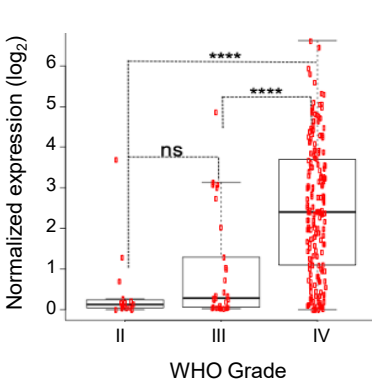
F
****
****
ns
Normalized expression (log2)
WHO Grade
II
III
IV

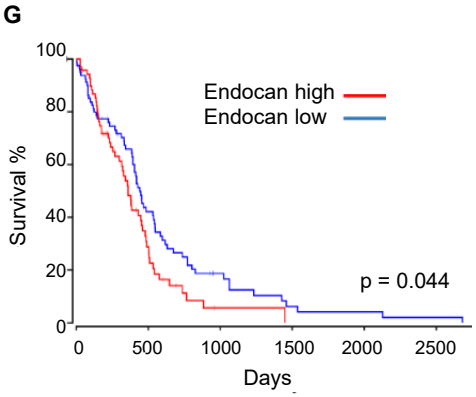
G
Endocan high
Endocan low
p = 0.044
Survival %
Days

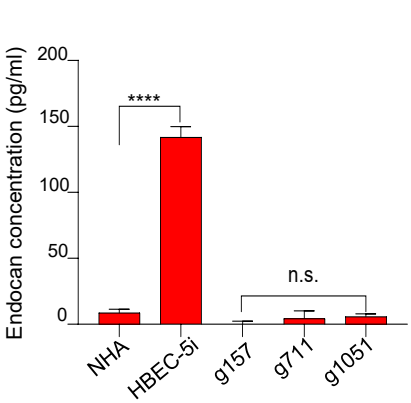
H
****
n.s.
Endocan concentration (pg/ml)
NHA
HBEC-5i
g157
g711
g1051

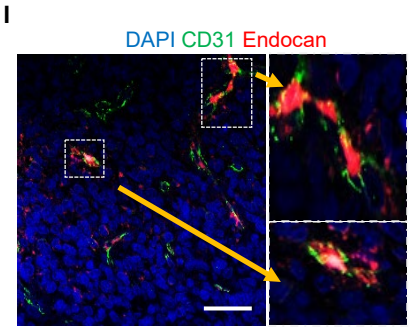
I
DAPI CD31 Endocan

Figure 2

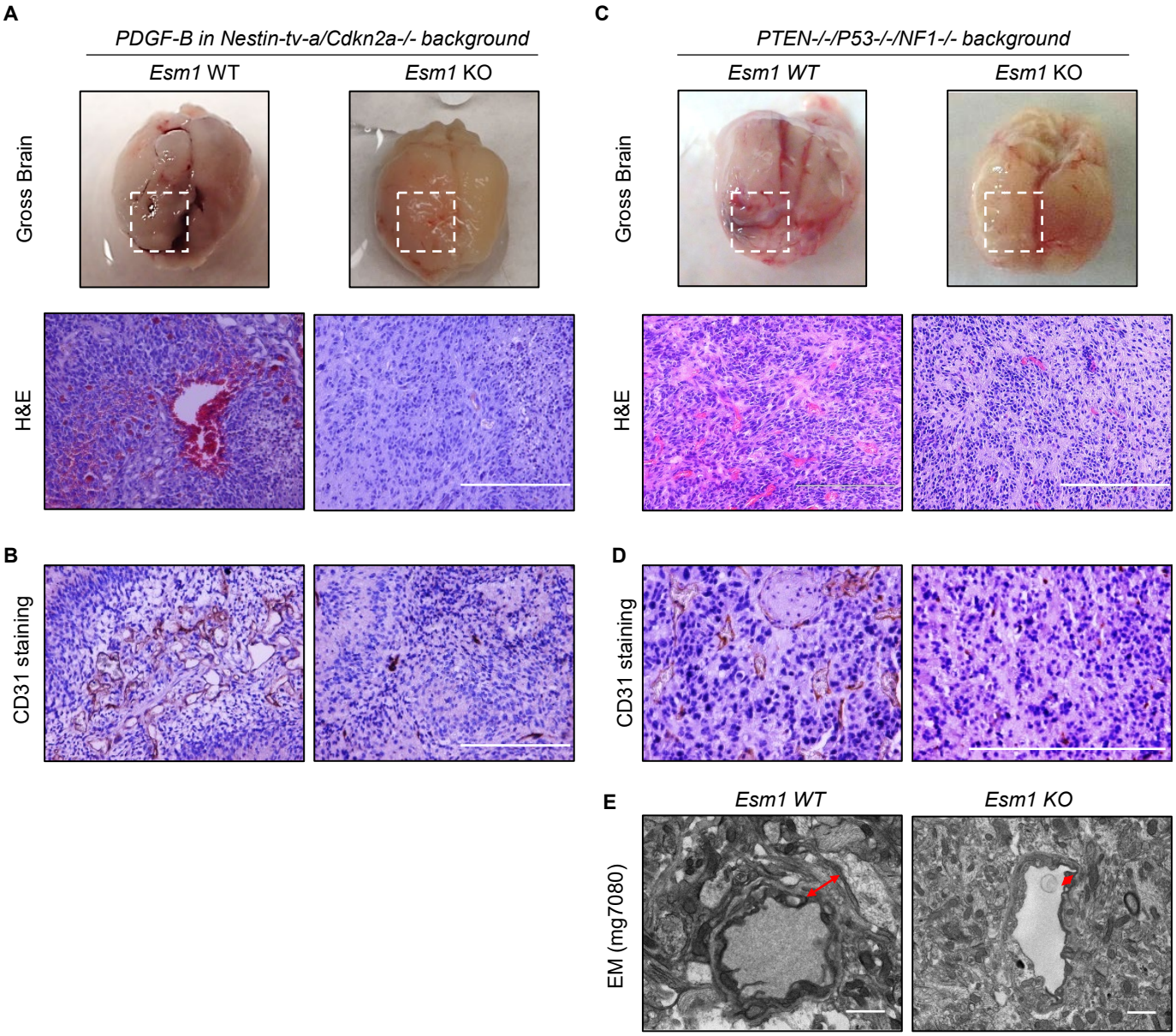
A
PDGF-B in Nestin-tv-a/Cdkn2a-/- background
Esm1 WT
Esm1 KO
Gross Brain
H&E
B
CD31 staining
C
PTEN-/-/P53-/-/NF1-/- background
Esm1 WT
Esm1 KO
Gross Brain
H&E
D
CD31 staining
E
Esm1 WT
Esm1 KO
EM (mg7080)

Figure 3

A

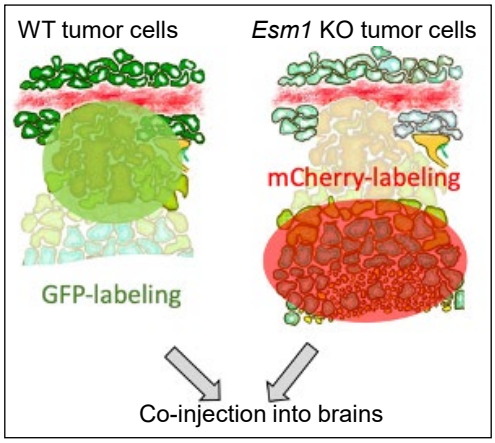

B

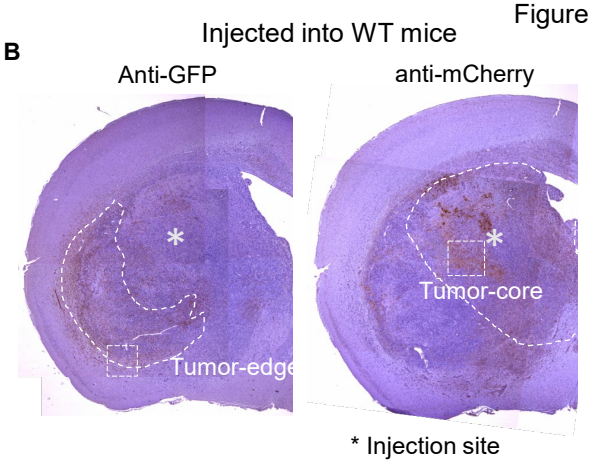

C

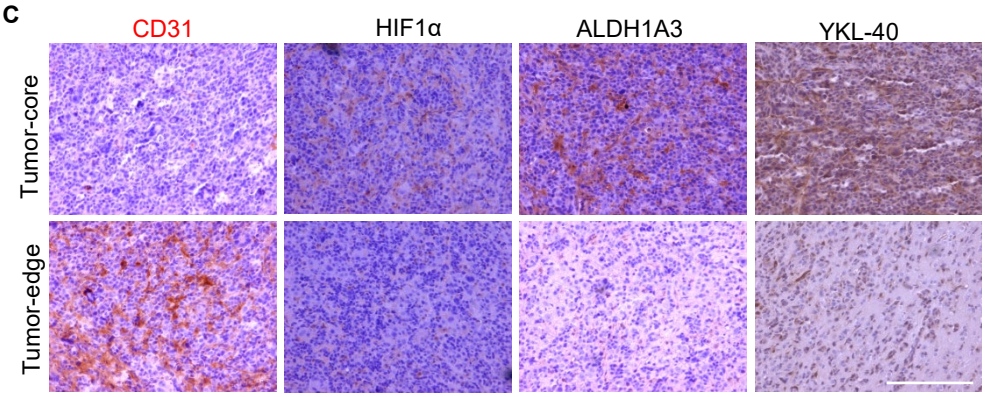

D

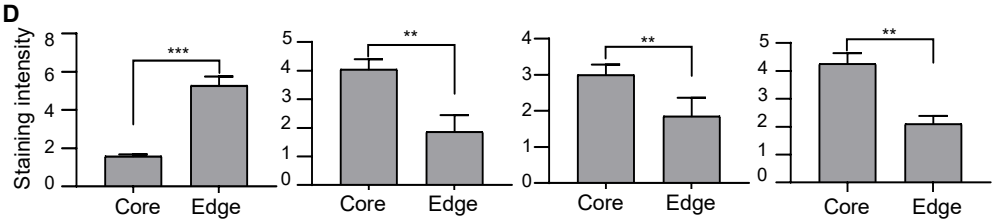

E

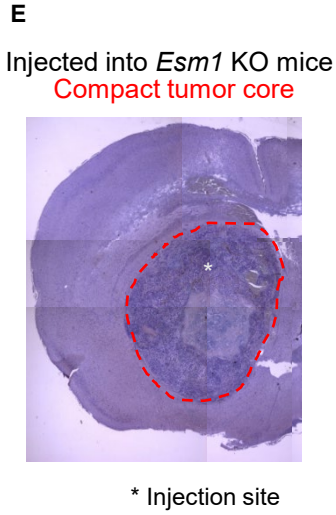

F

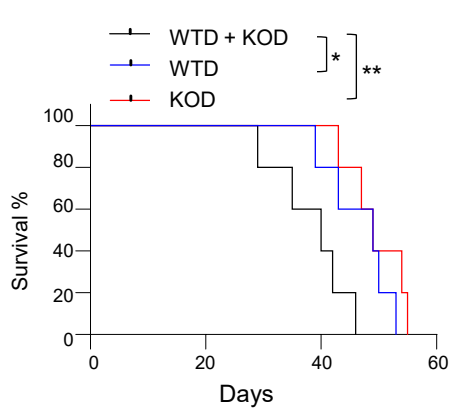

G

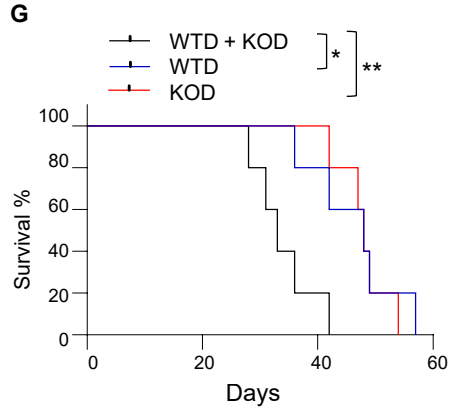

Figure 4

A

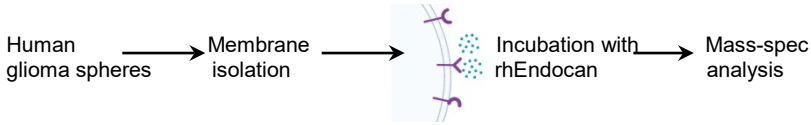

Platelet-derived growth factor receptor alpha

```
MGTSHPAFLV LGCLLTGLSL ILCQLSLPSI LPNENEKVVQ LNSSFSLRCF
GESEVSWQYP MSEEEESSDVE IRNEENNSGL FVTVLEVSSA SAAHTGLYTC
YYNHTQTEEN ELEGRHIYIY VPDPDVAFVP LGMTDYLVIV EDDDSAIIPC
RTTDPETPVT LHNSEGVVPA SYDSRQGFNG TFTVGPYICE ATVKGKKFQT
IPFNVYALKA TSELDLEMEA LKTVYKSGET IVVTCAVFNN EVVDLQWTYP
GEVKGKGITM LEEIKVPSIK LVYTLTVPEA TVKDSGDYEC AARQATREVK
EMKKVTISVH EKGFIEIKPT FSQLEAVNLH EVKHFVVEVR AYPPPRISWL
KNNLTLIENL TEITTDVEKI QEIRYRSKLK LIRAKEEDSG HYTIVAQNED
AVKSYTFELL TQVPSSILDL VDDHHGSTGG QTVRCTAEGT PLPDIEWMIC
KDIKKCNNET SWTILANNVS NIITEIHSRD RSTVEGRVTF AKVEETIAVR
CLAKNLLGAE NRELKLVAPT LRSELTVAAA VLVLLVIVII SLIVLVVIWK
QKPRYEIRWR VIESISPDGH EYIYVDPMQL PYDSRWEFPR DGLVLGRVLG
```

B

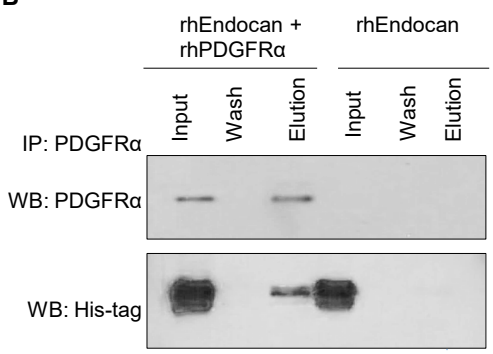

C

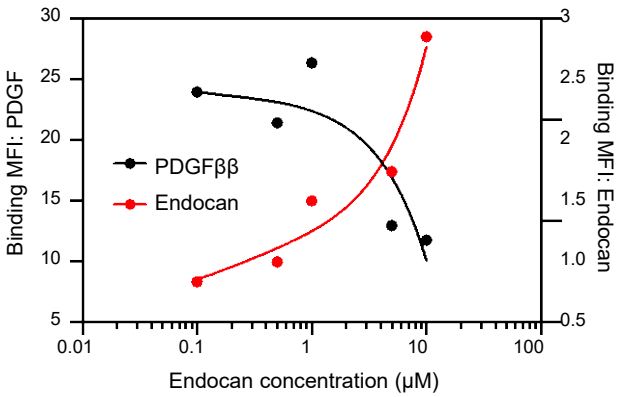

D

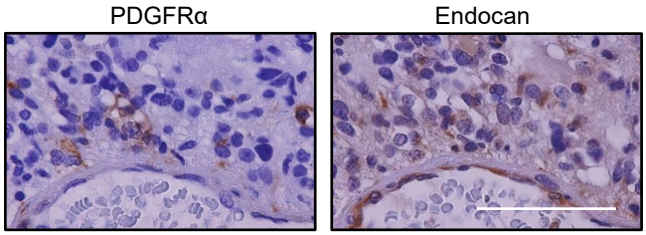

E

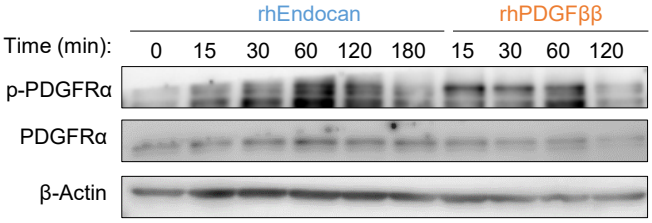

F

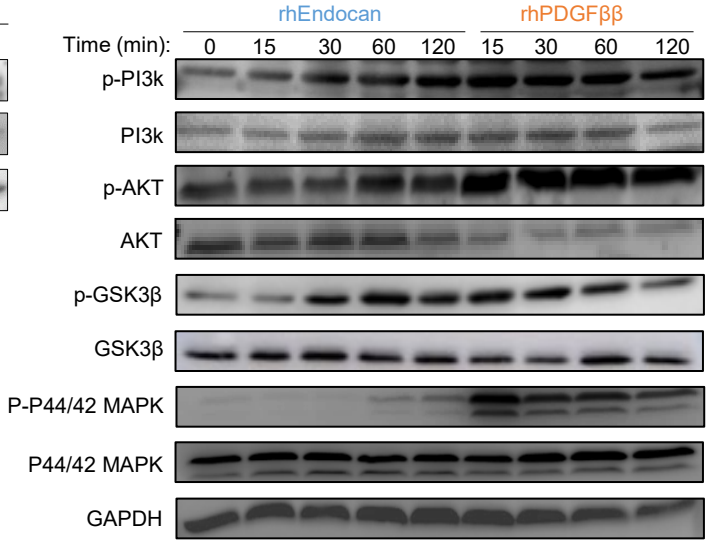

G

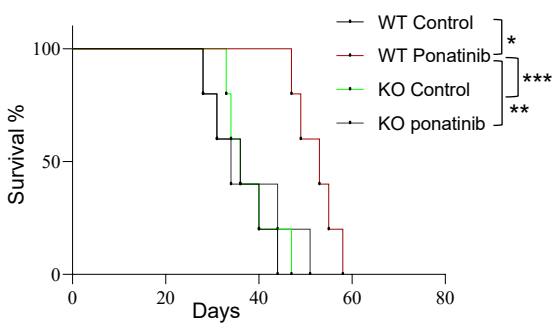

H

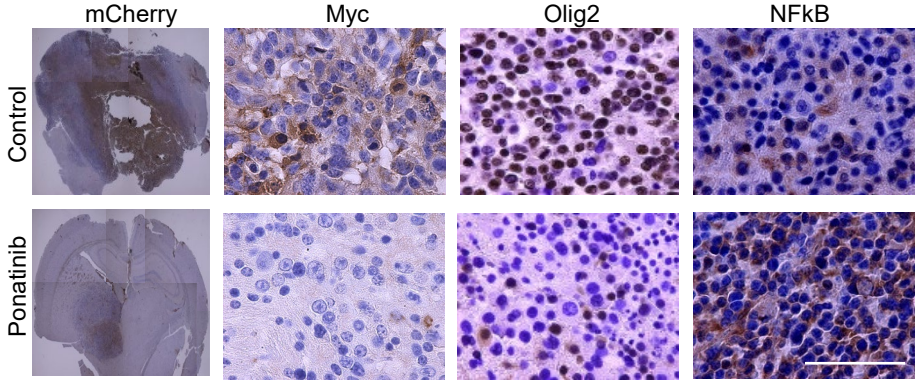

Figure 5

A

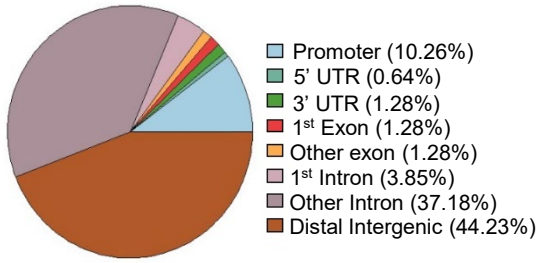

B

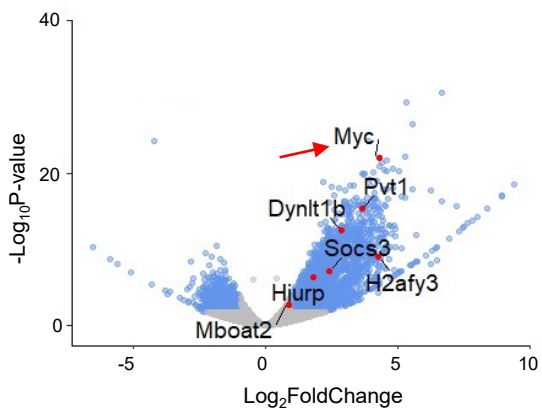

C

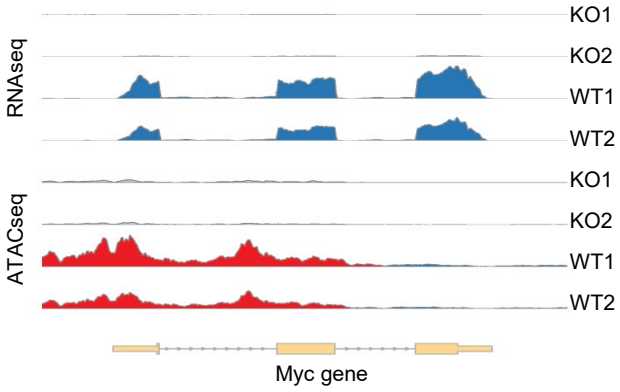

D

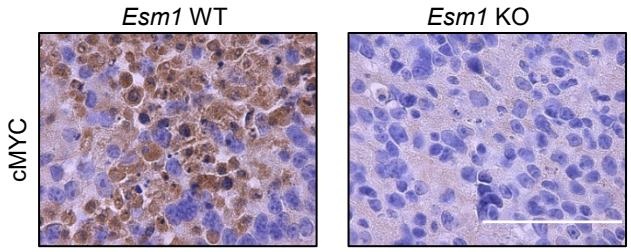

E

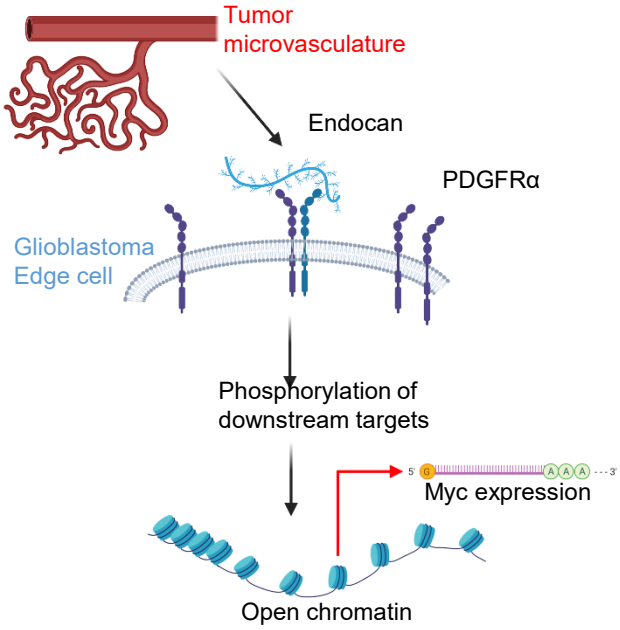

Figure 6

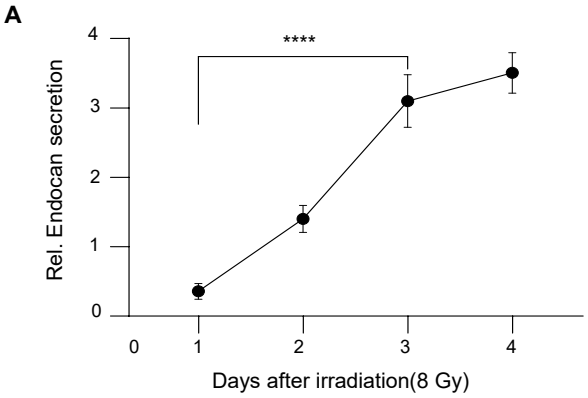
A
Rel. Endocan secretion
Days after irradiation(8 Gy)
****
0
1
2
3
4

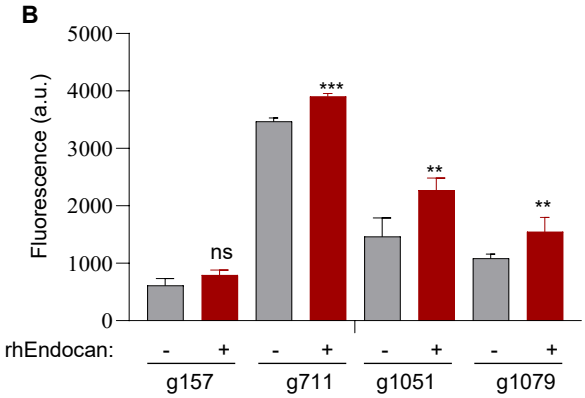
B
Fluorescence (a.u.)
5000
4000
3000
2000
1000
0
ns
***
**
**
rhEndocan:
-
+
g157
g711
g1051
g1079

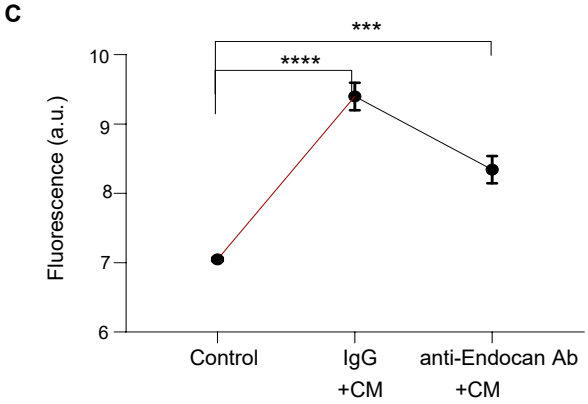
C
Fluorescence (a.u.)
***
****
10
9
8
7
6
Control
IgG +CM
anti-Endocan Ab +CM

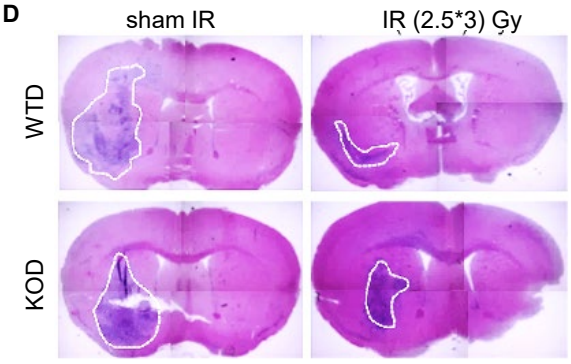
D
sham IR
IR (2.5*3) Gy
WTD
KOD

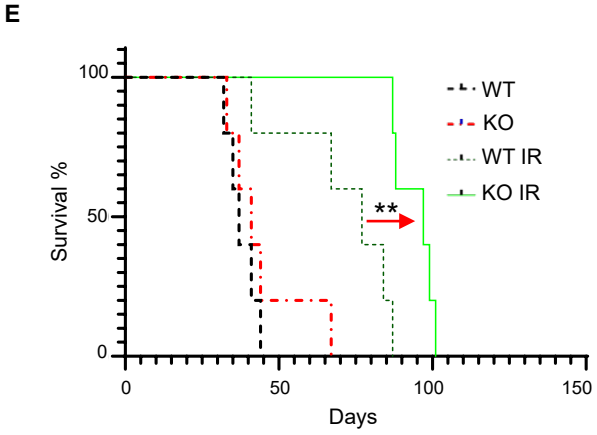
E
Survival %
Days
100
50
0
150
WT
KO
WT IR
KO IR
**

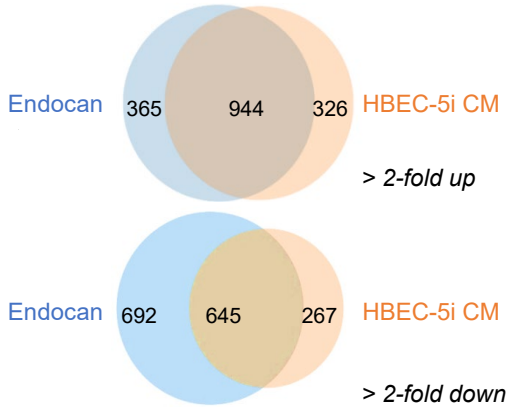
F
Endocan
365
944
326
HBEC-5i CM
> 2-fold up
Endocan
692
645
267
HBEC-5i CM
> 2-fold down

Figure 7

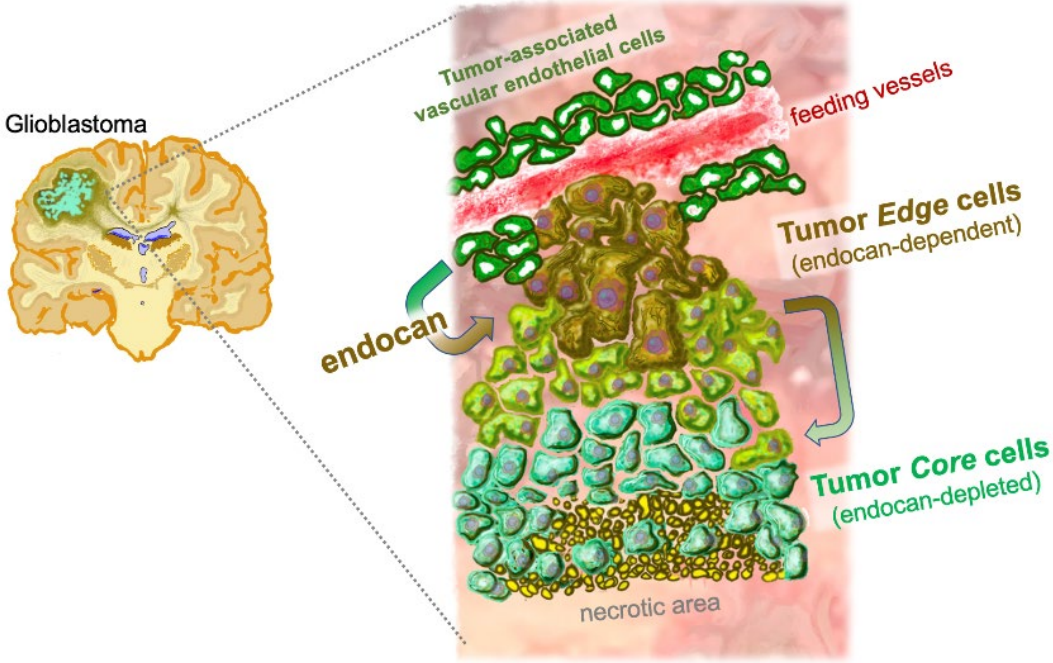
Glioblastoma
Tumor-associated
vascular endothelial cells
feeding vessels
Tumor Edge cells
(endocan-dependent)
endocan
Tumor Core cells
(endocan-depleted)
necrotic area

Supplementary Figure 1

A

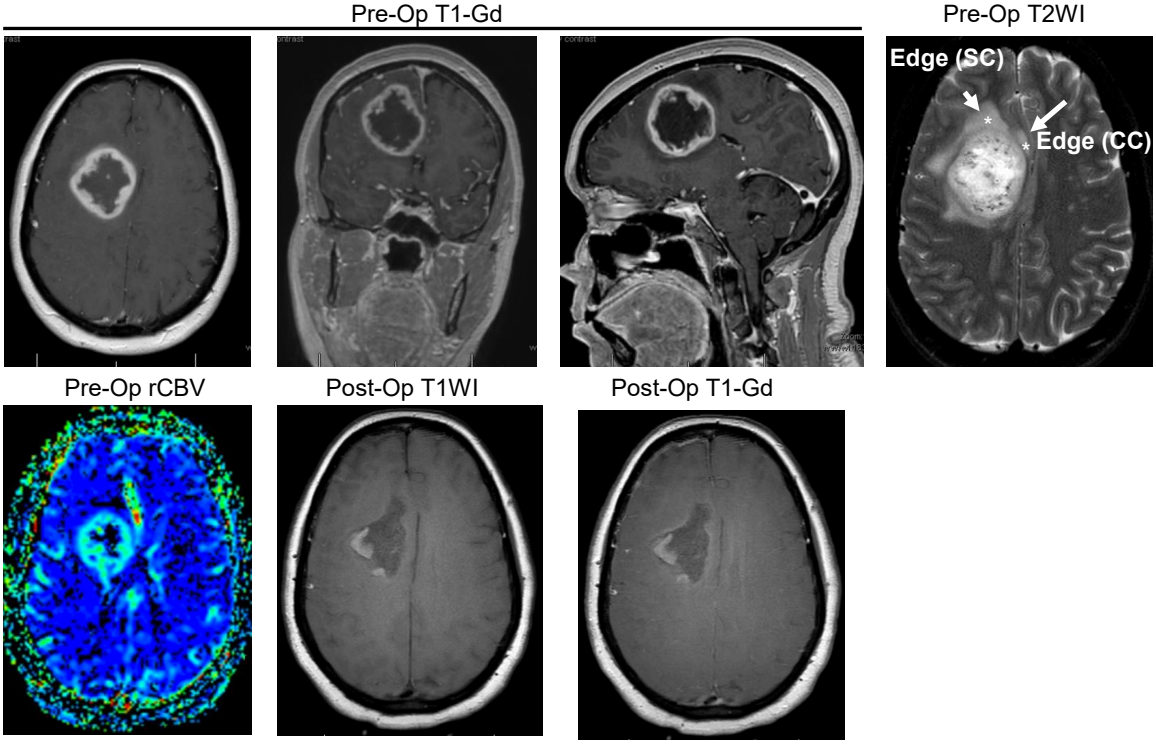

Supplementary Figure 2

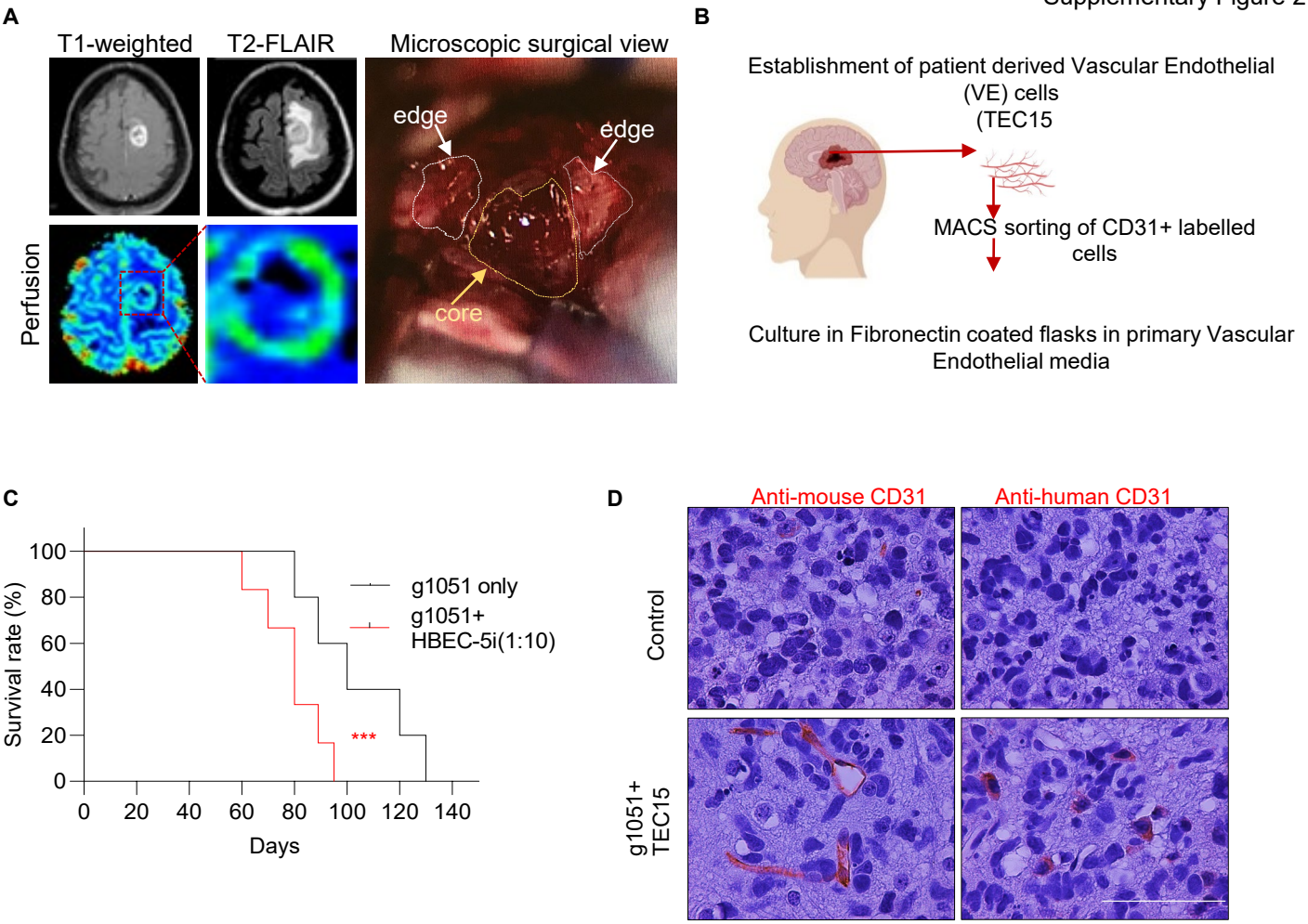

A

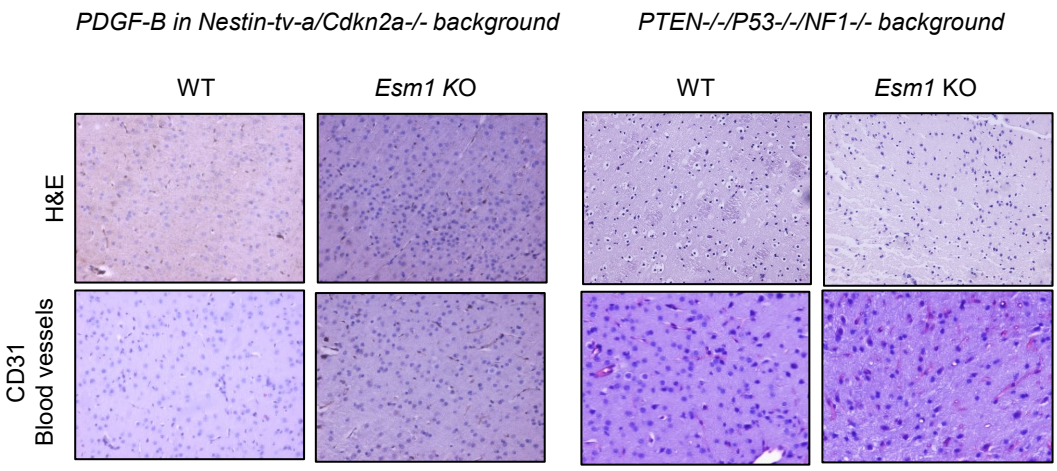
PDGF-B in Nestin-tv-a/Cdkn2a-/- background
PTEN-/-/P53-/-/NF1-/- background
WT
Esm1 KO
WT
Esm1 KO
H&E
CD31
Blood vessels

B

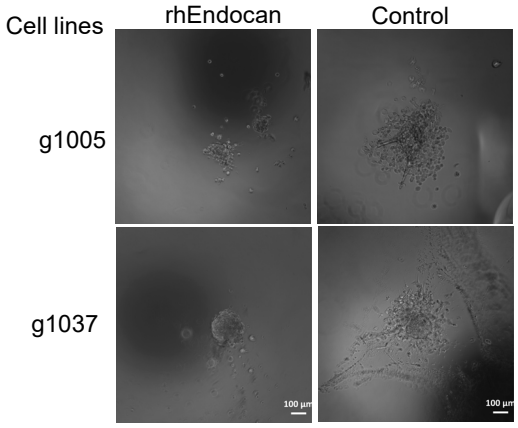
Cell lines
rhEndocan
Control
g1005
g1037
100 µm
100 µm

Supplementary Figure 4

A

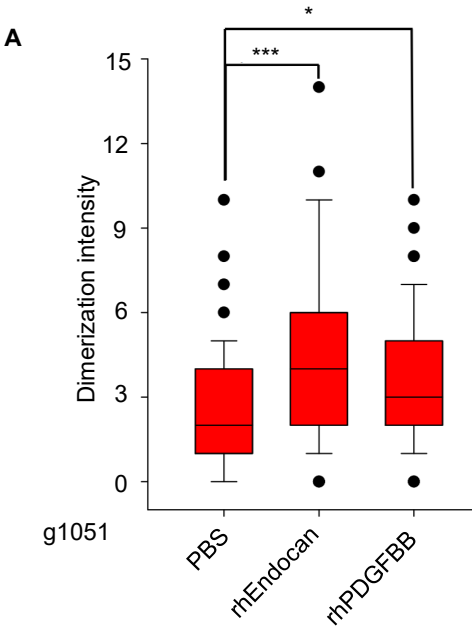

B

	X vs. PDGF	X vs. Endocan
Pearson r		
r	-0.9925	0.9957
95% confidence interval	-0.9933 to -0.9915	0.9952 to 0.9962
R squared	0.9850	0.9915
P value		
P (one-tailed)	<0.001	<0.001
P value summary	***	***
Significant? (alpha = 0.05)	Yes	Yes

C

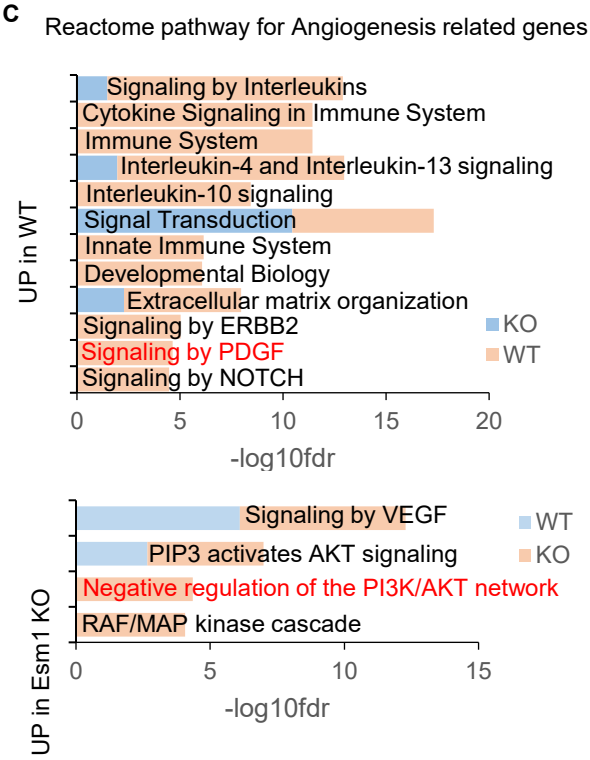

D

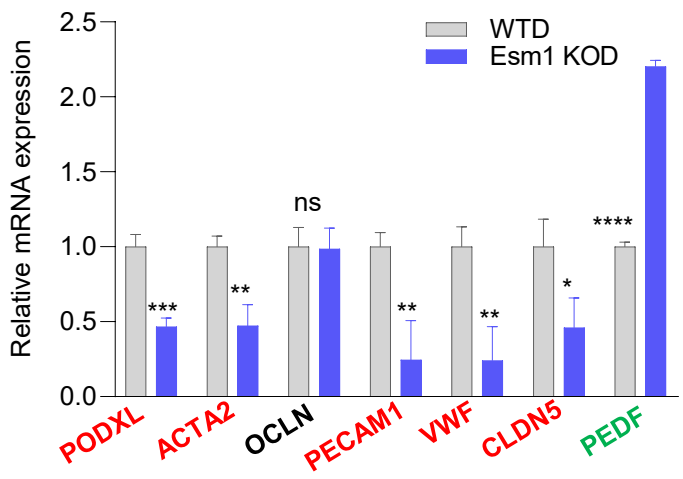

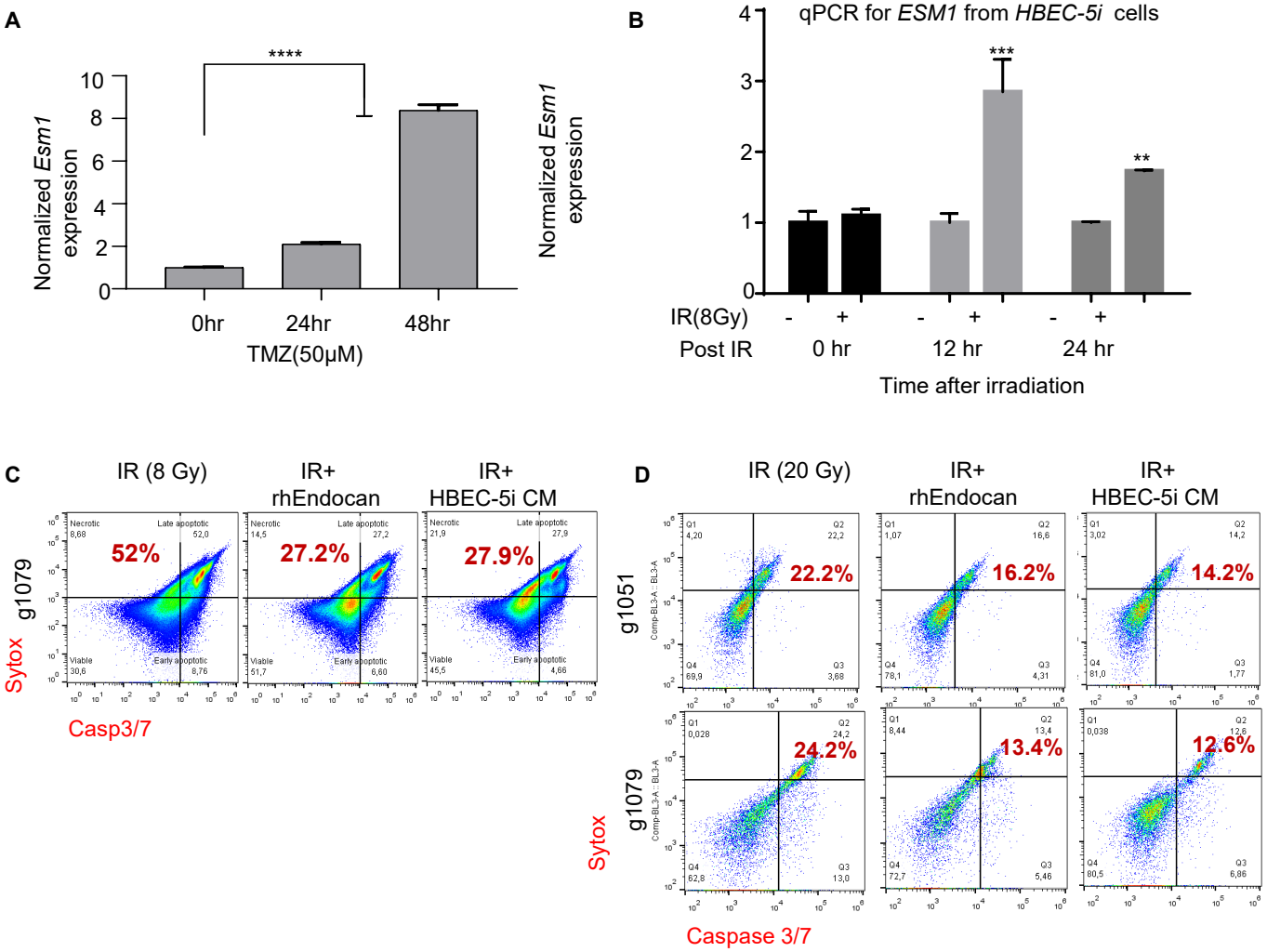
A
****
Normalized Esm1 expression
0hr
24hr
48hr
TMZ(50μM)
B
qPCR for ESM1 from HBEC-5i cells
***
**
IR(8Gy)
Post IR
0 hr
12 hr
24 hr
Time after irradiation
C
IR (8 Gy)
IR+ rhEndocan
IR+ HBEC-5i CM
52%
27.2%
27.9%
g1079
Sytox
Casp3/7
D
IR (20 Gy)
IR+ rhEndocan
IR+ HBEC-5i CM
22.2%
16.2%
14.2%
24.2%
13.4%
12.6%
g1051
g1079
Sytox
Caspase 3/7